

The VLT-UVES survey for molecular hydrogen in high-redshift damped Lyman- α systems: Physical conditions in the neutral gas

R. Srianand¹, Patrick Petitjean^{2,3}, Cédric Ledoux⁴, Gary Ferland⁵, Gargi Shaw⁵

¹ IUCAA, Post Bag 4, Ganesh Khind, Pune 411 007, India - email: anand@iucaa.ernet.in

² Institut d'Astrophysique de Paris – CNRS, 98bis Boulevard Arago, F-75014 Paris, France - email: petitjean@iap.fr

³ LERMA, Observatoire de Paris, 61 Avenue de l'Observatoire, F-75014, Paris, France

⁴ European Southern Observatory, Alonso de Córdova 3107, Casilla 19001, Vitacura, Santiago, Chile - email: cledoux@eso.org

⁵ Department of Physics and Astronomy, University of Kentucky, 177 Chemistry/Physics Building, Lexington, KY 40506
email: gary@pa.uky.edu and gargi@pa.uky.edu

Received date / Accepted date

ABSTRACT

We study the physical conditions in damped Lyman- α systems (DLAs), using a sample of 33 systems toward 26 QSOs acquired for a recently completed survey of H₂ by Ledoux et al. (2003). We use the column densities of H₂ in different rotational levels, together with those of C I, C I*, C I**, C II* and singly ionized atomic species to discuss the kinetic temperature, the density of hydrogen and the electronic density in the gas together with the ambient UV radiation field. Detailed comparisons are made between the observed properties in DLAs, the interstellar medium (ISM) of the Galaxy, the large and small Magellanic clouds (LMC and SMC).

The mean kinetic temperature of the gas corresponding to DLA subcomponents in which H₂ absorption line is detected, derived from the ortho-to-para ratio (153 ± 78 K), is higher than that measured in the ISM (77 ± 17 K) and the Magellanic clouds (82 ± 21 K). Typical pressure in these components (corresponding to $T = 100\text{--}300$ K and $n_{\text{H}} = 10\text{--}200$ cm⁻³), measured using C I fine-structure excitation, are higher than what is measured along ISM sightlines. This is consistent with the corresponding higher values for $N(\text{H}_2, J=2)/N(\text{H}_2, J=0)$ seen in DLAs. From the column densities of the high-J rotational levels, we derive that the typical radiation field in the H₂ bearing components is of the order of or slightly higher than the mean UV field in the Galactic ISM. Determination of electron density in the gas with H₂ and C I show the ionization rate is similar to that of a cold neutral medium (CNM) in a moderate radiation field. This, together with the fact that we see H₂ in 13-20% of the DLAs, can be used to conclude that DLAs at $z > 1.9$ could contribute as much as 50% star formation rate density seen in Lyman break galaxies (LBGs).

C II* absorption line is detected in all the components where H₂ absorption line is seen. The excitation of C II in these systems is consistent with the physical parameters derived from the excitation of H₂ and C I. We detect C II* in about 50% of the DLAs and therefore in a considerable fraction of DLAs that do not show H₂. In part of the later systems, physical conditions could be similar to that in the CNM gas of the Galaxy. However, the absence of C I absorption line and the presence of Al III absorption lines with a profile similar to the profiles of singly ionized species suggest an appreciable contribution from warm (WNM) and/or partially ionized gas. The absence of H₂, for the level of metallicity and dust depletion seen in these systems, are consistent with low densities (i.e. $n_{\text{H}} \leq 1$ cm⁻³) for a radiation field similar to the mean Galactic UV field.

Key words: Cosmology: observations – Galaxies: halos – Galaxies: ISM – Quasars: absorption lines

arXiv:astro-ph/0506555v1 23 Jun 2005

1 INTRODUCTION

Damped Ly- α (DLA) systems seen in QSO spectra are characterized by very large neutral hydrogen column densities: $N(\text{H I}) \gtrsim 2 \times 10^{20} \text{ cm}^{-2}$. Such an amount of neutral gas is usually measured through local spiral disks. The case for DLA systems to arise through proto-galactic disks is further supported by the fact that the cosmological density of the absorbing gas at $z_{\text{abs}} \sim 3$ is of the same order of magnitude as the cosmological density of stars at present epochs (Wolfe 1995). Moreover, the presence of heavy elements ($Z \sim 1/10Z_{\odot}$) suggests that DLAs are located in over-dense regions where star formation activity takes place (Pettini et al. 1997) and at low and intermediate redshifts strong metal line systems and DLAs have been demonstrated to be associated with galaxies (e.g. Bergeron & Boissé, 1991; Le Brun et al. 1997). It has also been shown that the profiles of the lines arising in the neutral gas show evidence for rotation (e.g. Prochaska & Wolfe 1997). However, hydrodynamical simulations have shown that the high redshift progenitors of present-day galactic disks could look like an aggregate of well separated dense clumps. In fact, the kinematics seen in the absorption line profiles of DLAs could be explained by relative motions of the clumps with little rotation (Haehnelt et al. 1998; Ledoux et al. 1998).

Studying the star-formation activities in DLAs is very important for the understanding of galaxy formation in the Universe. Recently, Wolfe et al. (2003a, 2003b, 2004) have shown that, even if DLAs sustain only a moderate star-formation activity, they will contribute appreciably to the global star-formation rate (SFR) density at high redshifts. The SFR in DLAs can be estimated either by detecting the galaxies responsible for DLAs or by inferring the intensity of the UV field in DLAs using the induced excitation of atomic and molecular species. In the latter case, it is important to have a clear understanding of the physical conditions in the gas to derive an accurate estimate of the SFR. In the case of the Galactic ISM, rotational excitations of H_2 (see Brown et al. 2002 and references there in) and fine-structure excitations of C I, C II, O I and Si II are used to derive the physical state of the absorbing gas (see for example Welty et al. 1999). Detecting and studying these transitions in DLAs is the first step toward understanding the physical conditions and hence the star-formation activity in DLAs.

Molecular hydrogen is ubiquitous in the neutral phase of the interstellar medium (ISM) of galaxies. Formation of H_2 is expected on the surface of dust grains, if the gas is cool, dense and mostly neutral, and from the formation of H^- ions if the gas is warm and dust-free (see e.g. Jenkins & Peimbert 1997; Cazaux & Tielens 2002). As the former process is most likely dominant in the neutral gas associated with DLA systems, it is possible to obtain an indirect indication of the dust content in DLAs without depending on extinction and/or heavy element depletion effects. Moreover, by determining the populations of different H_2 rotational levels, it is possible to constrain kinetic and rotational excitation temperatures and particle densities. Effective photo-dissociation of H_2 takes place in the energy range 11.1 – 13.6 eV through Lyman- and Werner-band absorption lines and the intensity of the local UV radiation field can therefore be derived from the observed molecular fraction. A direct determination of the local radiation field could have important implications in

bridging the link between DLA systems and star-formation activity at high redshifts.

We have searched for molecular hydrogen in DLA and sub-DLA systems at high redshift ($z_{\text{abs}} > 1.8$), using UVES at the VLT down to a detection limit of typically $N(\text{H}_2) \sim 2 \times 10^{14} \text{ cm}^{-2}$ (see Ledoux et al. 2003). Out of the 33 systems in our sample, 8 have firm and 2 have tentative detections of associated H_2 absorption lines. In all of the systems, we measured metallicities relative to Solar, $[\text{X}/\text{H}]$ (with either $\text{X}=\text{Zn}$, or S, or Si), and depletion factors of iron, $[\text{X}/\text{Fe}]$, supposedly onto dust grains. Although H_2 molecules are detected in systems with depletion factor, $[\text{Zn}/\text{Fe}]$, as low as 0.3, the systems where H_2 is detected are usually amongst those with the highest metallicities and depletion factors. In particular, H_2 is detected in the three systems with the largest depletion factors. Moreover, in two different systems, one of the H_2 -detected components has $[\text{Zn}/\text{Fe}] > 1.5$. This directly demonstrates that a large amount of dust is present in the components where H_2 is detected. The mean H_2 molecular fraction, $f = 2N(\text{H}_2)/[2N(\text{H}_2) + N(\text{H I})]$, in DLA systems is generally small (typically $\log f < -1$) and similar to what is observed in the Magellanic Clouds. There is no correlation between the amount of molecules and the neutral hydrogen column density; in particular, two systems where H_2 is detected have $\log N(\text{H I}) < 20.3$. Approximately 50 percent of the systems have $\log f < -6$: this is probably a consequence of a reduced formation rate of H_2 onto dust grains (probably because the gas is warm, $T > 1000 \text{ K}$) and/or of an enhanced ionizing flux relative to what is observed in our Galaxy.

In this work, we present additional high S/N ratio data on three of the DLA systems in which H_2 is detected and the results of multi-component Voigt profile fits to neutral and singly ionized species (including C I, C I* and C II*) in all the DLAs in our sample. We estimate the range of physical conditions in the neutral gas using standard techniques that are used in ISM studies. The paper is organized as follows. In Section 2, we give the details of the additional data and present the new fits to the H_2 absorption lines in the corresponding three systems. In Section 3, we discuss the relative populations of different H_2 rotational levels deriving information on the physical state of the gas by comparing the DLA observations with Galactic ISM, SMC, and LMC data. In Sections 4 and 5 we discuss, respectively, the fine-structure excitation of C I and the ionization state of Carbon. In Section 6 we study the C II* excitation in detail. Finally, we summarize our results and discuss various implications of the overall study in Section 7.

2 DATA SAMPLE

The Ultraviolet and Visible Echelle Spectrograph (UVES; Dekker et al. 2000), installed at the ESO VLT 8.2-m telescope unit Kueyen on Mount Paranal in Chile was used to search for H_2 in a large sample of DLAs. The sample and data reduction procedure are described in detail in Ledoux et al. (2003). Observations and details of Voigt profile analysis of H_2 and metal line absorption lines toward Q0013–004, Q0551–366 and Q1232+082, along the lines of sight of which H_2 is detected, are described in, respectively, Petitjean et al. (2002), Ledoux et al. (2002) and Srianand et al.

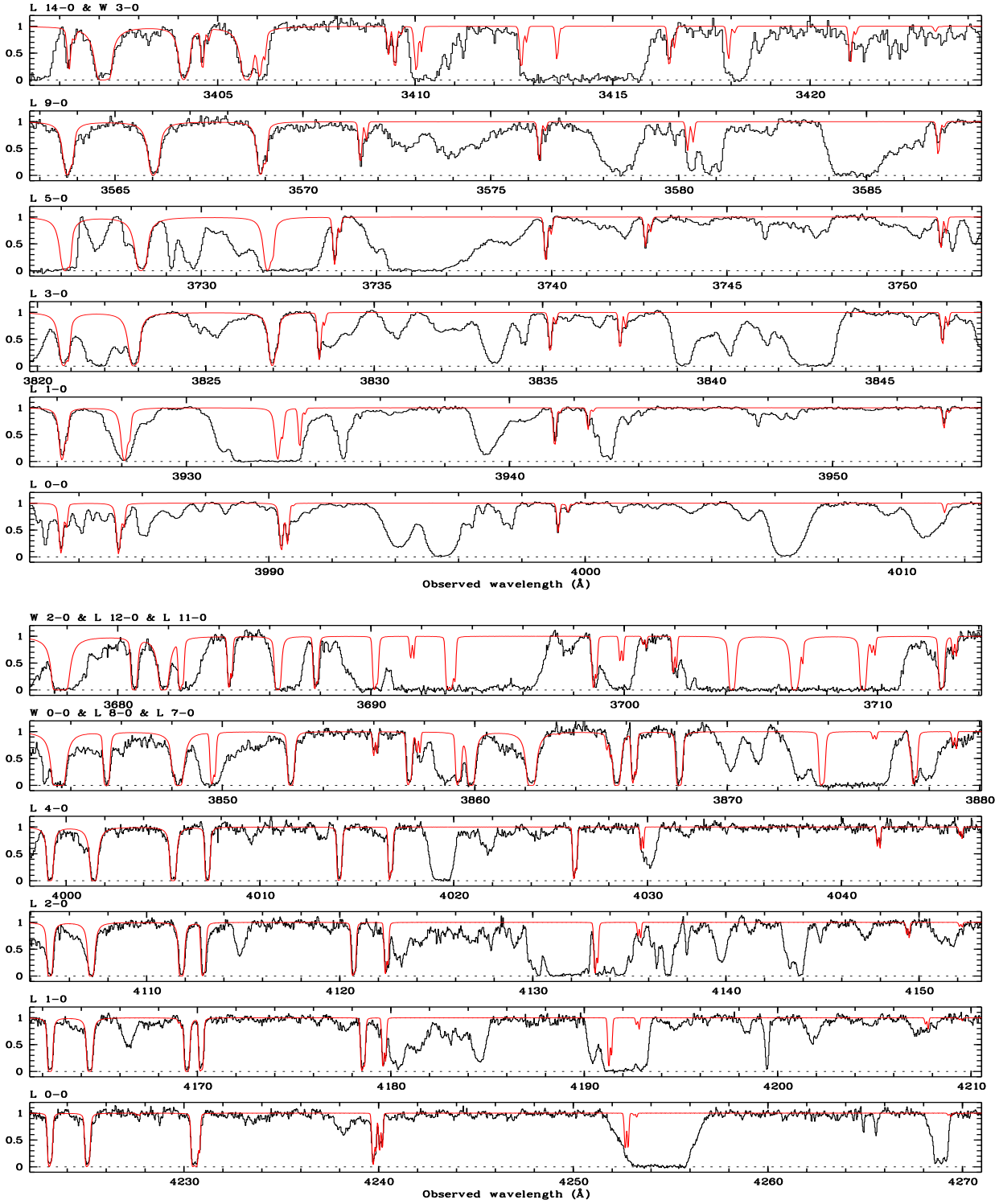


Figure 1. Voigt profile fits to different rotational levels in the ground vibrational state of H_2 detected at $z_{\text{abs}} = 2.5948$ toward Q 0405–443 (top panels) and $z_{\text{abs}} = 2.8111$ toward Q 0528–250 (bottom panels). The fit parameters are given in Table 1.

(2000). The Voigt profile fits to H_2 and other metal lines at $z_{\text{abs}} = 3.024$ toward Q 0347 – 383, $z_{\text{abs}} = 2.595$ toward Q 0405 – 443 and $z_{\text{abs}} = 2.0868$ toward Q 1444 + 014 are discussed in Ledoux et al. (2003). For systems in which H_2 is not detected, Ledoux et al. (2003) have provided upper lim-

its on $N(H_2)$ together with mean metallicities and depletion factors.

Recently, we have obtained additional higher spectral resolution spectra ($R \sim 55,000$) of Q 0347–383 and Q 0405 – 443 as a part of our ongoing programme on cos-

Table 1. Results of Voigt profile fitting to H₂ absorption lines using the new data

QSO	z_{abs}	J	$\log N$ (cm ⁻²)	b (km s ⁻¹)
Q 0405 – 443	2.59471	0	17.65 ^{+0.07} _{-0.15}	1.5±0.5
		1	17.97 ^{+0.05} _{-0.08}	
		2	15.93 ^{+0.75} _{-0.42}	
		3	14.81 ^{+0.14} _{-0.26}	
		4	≤ 13.55	
	2.59486	0	15.13 ^{+0.14} _{-0.10}	1.1±0.1
		1	15.24 ^{+0.13} _{-0.02}	
		2	14.00 ^{+0.01} _{-0.11}	
		3	13.93 ^{+0.09} _{-0.05}	
		4	≤ 13.55	
Q 0528 – 250	2.81100	0	17.29 ^{+0.08} _{-0.16}	2.8±0.5
		1	17.78 ^{+0.10} _{-0.15}	
		2	16.74 ^{+0.45} _{-0.46}	
		3	15.68 ^{+0.44} _{-0.17}	
		4	14.13 ^{+0.01} _{-0.01}	
	2.81112	0	13.68 ^{+0.01} _{-0.01}	1.0±0.3
		1	17.24 ^{+0.05} _{-0.07}	
		2	17.68 ^{+0.07} _{-0.04}	
		3	16.98 ^{+0.17} _{-0.36}	
		4	16.58 ^{+0.15} _{-0.59}	
	2.81112	0	14.32 ^{+0.50} _{-0.15}	1.0±0.3
		1	13.58 ^{+0.02} _{-0.04}	
		2	19.34 ^{+0.10} _{-0.10}	
		3	19.17 ^{+0.10} _{-0.10}	
		4	16.70 ^{+0.22} _{-0.22}	
Q 1232 + 082	2.33772	0	16.90 ^{+0.32} _{-0.32}	4.5±0.5
		1	14.68 ^{+0.05} _{-0.05}	
		2	14.45 ^{+0.04} _{-0.04}	
		3	14.45 ^{+0.04} _{-0.04}	
		4	14.45 ^{+0.04} _{-0.04}	

mic variation of the electron-to-proton mass ratio (Petitjean et al. 2004). Nine exposures of 1.5 h each were taken for each of the quasars over six nights under sub-arcsec seeing conditions in January 2002 and 2003 for Q 0347–383 and Q 0405 – 443, respectively. We have also obtained additional data of Q 1232+082 to study the HD lines that are detected in the DLA (Varshalovich et al. 2002). Spectra were reduced using the UVES pipeline and addition of individual exposures were performed using a sliding window and weighting the signal by the errors in each pixel. We detect a new H₂ component at $z_{\text{abs}} = 2.59486$ toward Q 0405–443 in addition to the strong component reported in Ledoux et al. (2003). We also present Voigt profile fits to the H₂ lines in the $z_{\text{abs}} = 2.811$ system toward Q 0528 – 250. The single H₂ component seen in the lower spectral resolution CASPEC spectrum (Srianand & Petitjean 1998) is resolved into two distinct components in our new UVES spectra. For both these systems the Voigt profile fits to the H₂ Lyman and Werner band absorption lines are shown in Fig. 1 and resulting parameters are summarised in Table 1. This Table also gives the results of Voigt profile fits to H₂ for the $z_{\text{abs}} = 2.33772$ toward Q 1232+082.

The main purpose of this paper is to provide a detail account of C I, C II* and other metal lines in DLAs of our sample and extract physical conditions in conjunction with the H₂ content reported in Ledoux et al. (2003). For the $z_{\text{abs}} = 2.139$ system toward Tol 1037+014 and the

$z_{\text{abs}} = 3.350$ system toward Q 1117 – 1329, we use the results presented in Srianand & Petitjean (2001) and Péroux et al. (2002) respectively. For the rest of the systems we give here the results of the multicomponent Voigt profile fits. For this we use a Voigt-profile fitting code that determines the best fitting parameters (column density, velocity dispersion and redshift) using χ^2 minimization techniques (Chand et al. 2004). We use the oscillator strengths compiled in Table 1 of Ledoux et al. (2003) for metal ions and those given by Morton & Dinerstein (1976) for H₂. In this article, we measure metallicities relative to Solar, $[X/H] \equiv \log[N(X)/N(H)] - \log[N(X)/N(H)]_{\odot}$, with either X=Zn, or S, or Si, and depletion factors of iron, $[X/Fe] \equiv \log[N(X)/N(Fe)] - \log[N(X)/N(Fe)]_{\odot}$, adopting the Solar abundances from Savage & Sembach (1996).

3 DETERMINATION OF PHYSICAL PARAMETERS USING H₂ LEVEL POPULATION

In this section, we estimate different physical parameters from the column densities of H₂ in different J rotational levels.

3.1 Kinetic temperature of the gas

It is a standard procedure, in ISM studies, to use the ortho-to-para ratio (OPR) to infer the kinetic temperature of the gas assuming local thermodynamic equilibrium, LTE (Tumlinson et al. 2002, and references there in). Indeed, recent numerical investigations suggest that the OPR is a good tracer of the kinetic temperature over large regions of the parameter space (Shaw et al. 2004). For completeness, we first review our understanding of the OPR and outline the method for deriving the kinetic temperature before applying the method to the data.

3.1.1 General outline

As the interconversion between para and ortho states involves a spin flip, it is not allowed for processes involving an isolated molecule (i.e., radiative processes cannot induce interconversion). Ortho/para interconversion is only possible through (i) spin exchange induced by collisions with protons (with a rate coefficient in the range $10^{-10} - 10^{-9}$ cm³s⁻¹; see Dalgarno, Black & Weisheit 1973; Flower & Watt 1984 and Gerlich 1990) or with hydrogen atoms (with a rate coefficient an order of magnitude less than that of protons; Mandy & Martin 1993; Tiné et al. 1997) and (ii) reactions on the surface of dust grains (Le Bourlot 2000). In the case of local thermodynamic equilibrium (LTE),

$$\text{OPR}_{\text{LTE}} = 3 \frac{\sum_{J=\text{odd}} (2J+1) \exp[-BJ(J+1)/T]}{\sum_{J=\text{even}} (2J+1) \exp[-BJ(J+1)/T]} \quad (1)$$

where, J, is the rotational quantum number, B is the rotational constant of H₂ ($B = 85.3$ K), and T is either the kinetic temperature of the gas (when OPR is governed by spin-exchange collisions) or the formation temperature (when OPR is governed by H₂ formation on the surface of dust

Table 2. Excitation temperatures measured in individual H_2 components of DLAs in the sample of Ledoux et al. (2003)

QSO	z_{abs}	$\log N(\text{H I})^a$	$\log N(\text{H}_2)$	T_{01} (K)	T_{02} (K)	T_{13} (K)	OPR	$T(\text{OPR})$ (K)
Q 0013 – 004	1.96685	20.83(0.05)	$16.38^{+0.03}_{-0.04}$	300^{+276}_{-96}	766^{+584}_{-244}	395^{+59}_{-45}	1.85 ± 0.28	114^{+14}_{-12}
	1.96822		$16.54^{+0.05}_{-0.05}$	73^{+7}_{-8}	302^{+33}_{-30}	519^{+59}_{-75}	0.64 ± 0.09	66^{+3}_{-4}
Q 0347 – 383	3.02489	20.73(0.05)	$14.55^{+0.09}_{-0.09}$...	740^{+499}_{-212}	558^{+100}_{-73}	3.45 ± 0.47	≥ 200
Q 0405 – 443	2.59471	21.05(0.10)	$18.14^{+0.07}_{-0.12}$	121^{+10}_{-10}	101^{+24}_{-24}	104^{+4}_{-4}	2.10 ± 0.30	127^{+19}_{-15}
	2.59486		$15.51^{+0.15}_{-0.07}$	91^{+6}_{-6}	118^{+5}_{-5}	219^{+19}_{-19}	1.34 ± 0.17	93^{+6}_{-7}
Q 0528 – 250	2.81100	21.35(0.07)	$17.93^{+0.14}_{-0.20}$	167^{+7}_{-7}	190^{+46}_{-46}	156^{+11}_{-11}	2.47 ± 0.36	152^{+50}_{-24}
	2.81112		$17.90^{+0.11}_{-0.14}$	138^{+12}_{-12}	238^{+46}_{-46}	278^{+57}_{-57}	1.83 ± 0.33	113^{+17}_{-13}
Q 0551 – 366	1.96168	20.70(0.08)	$15.64^{+0.40}_{-0.14}$	76^{+7}_{-7}	248^{+52}_{-52}	401^{+73}_{-73}	0.90 ± 0.16	76^{+8}_{-6}
	1.96214		$17.40^{+0.65}_{-0.93}$	175^{+88}_{-88}	326^{+65}_{-65}	446^{+185}_{-185}	1.74 ± 0.72	108^{+42}_{-28}
	1.96221		$15.58^{+0.03}_{-0.12}$	154^{+24}_{-24}	415^{+25}_{-25}	593^{+39}_{-39}	1.86 ± 0.23	115^{+13}_{-14}
Q 1232 + 082	2.33772	20.90(0.08)	$19.57^{+0.12}_{-0.12}$	67^{+12}_{-12}	67^{+6}_{-6}	148^{+22}_{-22}	0.73 ± 0.32	71^{+12}_{-16}
Q 1444 + 014	2.08680	20.25(0.07)	$16.49^{+0.28}_{-0.11}$	285^{+35}_{-35}	205^{+15}_{-15}	196^{+14}_{-14}	3.59 ± 0.42	≥ 200
	2.08696		$18.15^{+0.15}_{-0.15}$	193^{+8}_{-8}	148^{+37}_{-37}	120^{+1}_{-1}	3.20 ± 0.28	≥ 200

Note: The $z_{\text{abs}} = 1.97296$ and 1.97380 components toward Q 0013–004 are not considered here as the H_2 column densities of the $J = 0$ and $J = 1$ levels are not known accurately due to saturation effects (see Petitjean et al. 2002)

^a Integrated H I column density in all the components (with and without H_2).

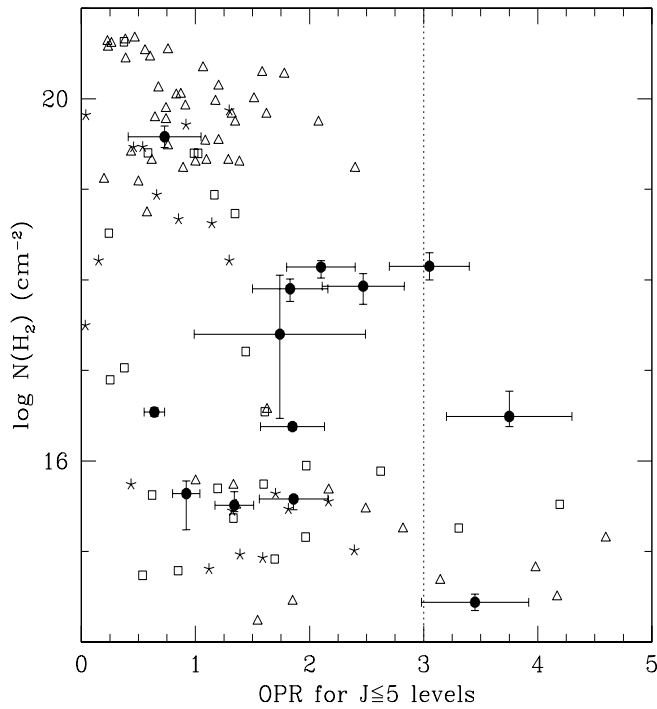


Figure 2. The Ortho-to-Para ratio (OPR) obtained using the populations of the $J \leq 5$ rotational levels in individual components of DLAs (black dots) is plotted against the total H_2 column density. Other data points are from Savage et al. (1977), Spitzer, Cochran & Hirshfeld (1974) for the Galactic ISM (triangles), and Tumlinson et al. (2002) for the LMC (squares) and SMC (asterisks). The vertical short-dashed line shows the high temperature LTE limit of the OPR (i.e., $\text{OPR} = 3$).

grains with LTE distribution characterized by the formation temperature T_{form} ; see Sternberg & Neufeld 1999; Takahashi 2001). The equilibrium temperature, $T(\text{OPR})$, can be obtained using the observed value of OPR and Eq. 1. This

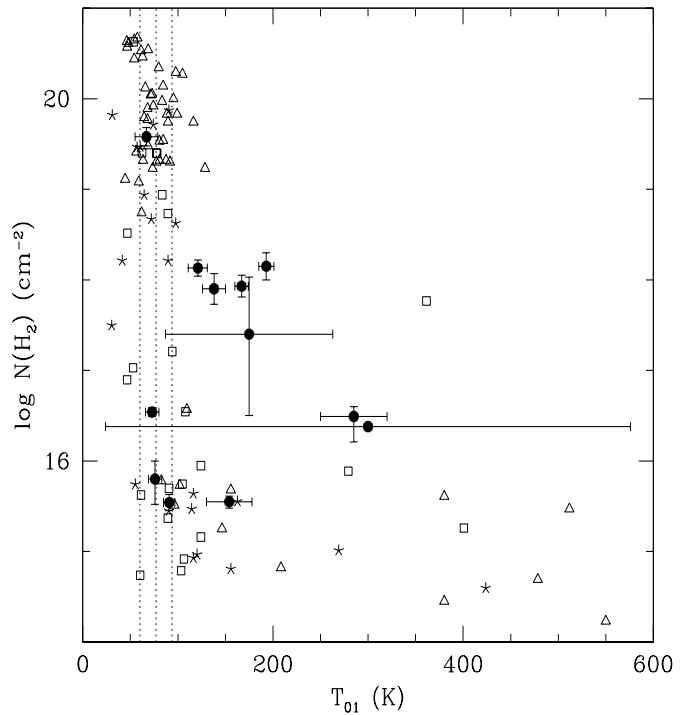


Figure 3. The rotational temperature T_{01} obtained from the $N(J=1)/N(J=0)$ ratio in DLAs (black dots) is plotted against the total column density of molecular hydrogen. Other data points are from Savage et al. (1977), Spitzer, Cochran & Hirshfeld (1974) for the Galactic ISM (triangles), and Tumlinson et al. (2002) for the LMC (squares) and SMC (asterisks). The vertical short-dashed lines show the mean and 1σ range of T_{01} measured by Savage et al. (1977) in the Galactic ISM.

will trace the kinetic temperature of the gas if spin-exchange collisions are mainly responsible for the observed OPR.

If the gas is dense and cold and if most of the H_2 molecules are in the $J = 0$ and $J = 1$ levels then,

$$\text{OPR}_{\text{LTE}} \sim \frac{N(J=1)}{N(J=0)} = 9 \times \exp(-170.5/T_{01}). \quad (2)$$

In the case of very optically thick molecular gas for which there is enough self-shielding, the $N(J=1)/N(J=0)$ ratio can be maintained at its Boltzmann value and the excitation temperature, T_{01} , equals the kinetic temperature. Savage et al. (1977) measured a mean excitation temperature, $T_{01} = 77 \pm 17$ K, for the galactic ISM. This is consistent with the mean temperature of the ISM measured using 21 cm absorption lines. Thus it is widely believed that when there is sufficient shielding (i.e. $\log N(\text{H}_2) \text{ cm}^{-2} \geq 16.5$), T_{01} is a reasonably good tracer of the kinetic temperature. This is because in the shielded region, H_2 photodissociation time-scale can be larger than the time-scale for charge exchange collision (Flower & Watt, 1984). Also a recent multi-wavelength study of Galactic sightlines show the T_{01} measured in optically thick cases closely follow the spin temperature measured from 21 cm observations (see Roy et al 2005).

The excitation temperature, T_{ij} , between different rotational levels (say $J=i$ and j) of a given species (either ortho or para H_2) can be obtained using,

$$\frac{N(J=j)}{N(J=i)} = \frac{2j+1}{2i+1} \exp(-B[j(j+1) - i(i+1)]/T_{ij}). \quad (3)$$

Unlike OPR, this ratio can be altered by radiation pumping and formation pumping in addition to collisions. If collisions dominate the rotational excitation then T_{ij} will be equal to $T(\text{OPR})$. Presence of formation pumping and/or UV pumping will make $T_{ij} > T(\text{OPR})$. In the following section we discuss various temperature estimates from the DLA sample.

3.1.2 Kinetic temperature of the H_2 components

In our sample, H_2 is only detected in $J \leq 5$ levels of the vibrational ground state. Thus we compute the OPR by summing the H_2 column densities for levels with $J \leq 5$. The observed value of the OPR for each DLA is given in column #8 of Table 2. We calculate $T(\text{OPR})$ from the measured OPR for individual systems using Eq. 1 (see column #9 of Table 2). When the kinetic temperature (or formation temperature) is high (i.e., $T \geq 200$ K) the OPR reaches 3, the value expected based on spin statistics. For a kinetic temperature similar to that seen in the cold neutral medium of our Galaxy ($\simeq 80$ K) the expected OPR under LTE assumption is less than 1. From Table 2, it is clear that the LTE temperatures measured from the OPR for DLAs are most of the times higher than 80 K (the mean found in the Galactic ISM.)

In Fig. 2 we plot the observed values of the OPR against the total H_2 column density in the ISM (triangles), LMC (squares), SMC (asterisks) and DLAs (circles with error-bars). It is apparent that most of the OPR values in DLAs are significantly different from 3 (see also column #8 of Table 2). The distribution of the OPR as a function of $N(\text{H}_2)$ in DLAs is consistent with that observed along Galaxy, LMC and SMC sightlines (see Fig. 2) when $\log N(\text{H}_2) \leq 16$ and for rest of the components OPR in DLAs are systematically higher than that measured in the Galaxy, LMC and SMC. For example, $\text{OPR} \geq 3$ is seen only along sightlines with low H_2 optical depth (i.e. $N(\text{H}_2) \leq 10^{16} \text{ cm}^{-2}$) in the Galaxy, LMC and SMC (see Fig. 2). On the contrary, out of the three

DLA components with $\text{OPR} \geq 3$, two, at $z_{\text{abs}} = 2.08680$ and $z_{\text{abs}} = 2.08692$ toward Q 1444+014, are optically thick in the Lyman band absorption lines.

We next investigate the dependence of T_{01} (measured using Eq. 2) on the total H_2 column density (see Fig 3). Individual values measured in DLAs are listed in Table 2 (see column #5). The large errors on both $N(\text{H}_2)$ and T_{01} are mostly a consequence of the difficulty to measure the Doppler parameter when the lines are saturated. In the case of the $z_{\text{abs}} = 1.96685$ component toward Q 0013 – 004 the uncertainty is a consequence of line blending (see Petitjean et al. 2002). The vertical dotted lines show the mean and 1σ range of T_{01} measured by Savage et al. (1977). The data points from the Magellanic clouds (Tumlinson et al. 2002) are consistent with this range (mean $T_{01} = 82 \pm 21$ K). As in the case of the OPR, most of the measurements from DLAs with optically thick H_2 (i.e. $\log N(\text{H}_2) \geq 16.5$) are well separated from that of the ISM and Magellanic clouds (Fig. 3) and the spread seen in the optically thin case is consistent with that seen in local ISM. Note that the system with lowest molecular content ($z_{\text{abs}} = 3.02489$ toward 0347 – 383) has $N(J=0)$ an order of magnitude lower than $N(J=1)$. T_{01} can not be computed in this case as the maximum expected column density ratio, $N(J=1)/N(J=2)$, is 9 under LTE conditions (see Eq. 2). For the high optical depth clouds (i.e. $\log N(\text{H}_2) \text{ cm}^{-2} \geq 16.5$) in DLAs the mean T_{01} is 153 ± 78 K. In most of the components the two temperatures T_{01} and $T(\text{OPR})$ are consistent within errors. This is mainly because most of the H_2 molecules reside in the ground states.

In summary, if we assume LTE then $T(\text{OPR})$ and T_{01} measured in DLAs (with $\log N(\text{H}_2) \geq 16.5$) at high redshift are on an average higher than that measured in the ISM, LMC and SMC sightlines. In this high $N(\text{H}_2)$ range T_{01} is expected to trace the kinetic temperature. However, in the case of optically thin systems the $T(\text{OPR})$ (or T_{01}) measured in DLAs are consistent with that measured in LMC, SMC and Galactic sightlines. Under the LTE assumption we find that H_2 components in DLAs have kinetic temperatures in the range 100–200 K.

3.2 Rotational excitation

The rotational level populations are affected by particle collisions, UV pumping, and formation pumping. While the collisional excitation plays a significant role in populating the low- J levels, those with $J \geq 3$ are usually populated by formation processes and UV pumping. In what follows, we discuss the excitation of H_2 as seen in DLAs and compare with ISM, LMC and SMC sightlines.

3.2.1 Low- J excitation

The collisional contribution to the excitation of H_2 can be investigated by studying the $N(J=2)/N(J=0)$ and $N(J=3)/N(J=1)$ ratios. In general $J=2$ and $J=3$ levels can also be populated by deexcitation of H_2 formed in the high- J states (usually referred to as formation pumping) or through UV pumping. The collisional excitation rate for the $J=0 \rightarrow 2$ transition is about an order of magnitude higher than that of the $J=1 \rightarrow 3$ transition for kinetic temperatures in the range 100 to 300 K (Forrey et al. 1997). The spontaneous decay rate from $J=3$ is an order of magnitude smaller

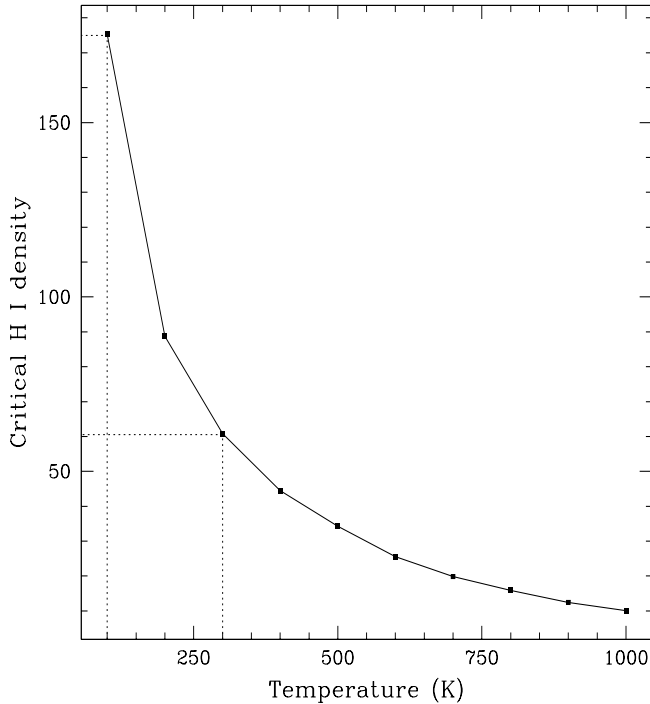


Figure 4. Critical hydrogen density (n_H) as a function of kinetic temperature for the thermalization of the $J = 0$ and 2 levels. The curve is obtained by equating the collisional de-excitation and spontaneous decay rates. We have used the collisional rates at low temperature given by Forrey et al. (1997). The spontaneous decay rates are from Turner et al. (1977). It is clear from the short-dashed lines that for $100 \leq T \leq 300$ K the critical density is $175 \geq n_H \text{ (cm}^{-3}\text{)} \geq 60$.

that from $J = 2$. This means that the ground and first excited states of para- H_2 can be thermalized at lower densities compared to that of ortho- H_2 . In Fig. 4, we plot as a function of temperature the critical hydrogen density for which the collisional deexcitation rate becomes equal to the spontaneous decay rate for the $J=2 \rightarrow J=0$ transition. It is clear from this figure that the hydrogen density has to be high (in the range $60\text{--}175 \text{ cm}^{-3}$) in order for the $N(J=2)/N(J=0)$ ratio to be equal to the LTE value corresponding to typical kinetic temperatures inferred from the OPR (i.e 100 to 300 K).

In Fig. 5 we plot the ratio, $N(J=2)/N(J=0)$, observed in DLAs, the Galaxy, LMC and SMC as a function of the total H_2 column density. The vertical dotted lines in the figure shows the expected values of the ratio for four different excitation temperatures assuming LTE. Values of the excitation temperature T_{02} for individual DLA H_2 components obtained using Eq. 3 are given in Table 2. The observed excitation temperatures are in the range 100 to 600 K with most of them at $T_{02} \simeq 150\text{--}300$ K. If the level populations are in LTE then the required hydrogen density to maintain the equilibrium is $65\text{--}150 \text{ cm}^{-3}$ (see Fig. 4). We can see from Fig. 5 that in DLAs where H_2 is optically thick, the $N(J=2)/N(J=0)$ ratio is larger than that seen in similar gas of the Galactic ISM, LMC and SMC. It can be seen from Table 2 that, in most of the DLAs, T_{01} is lower than or

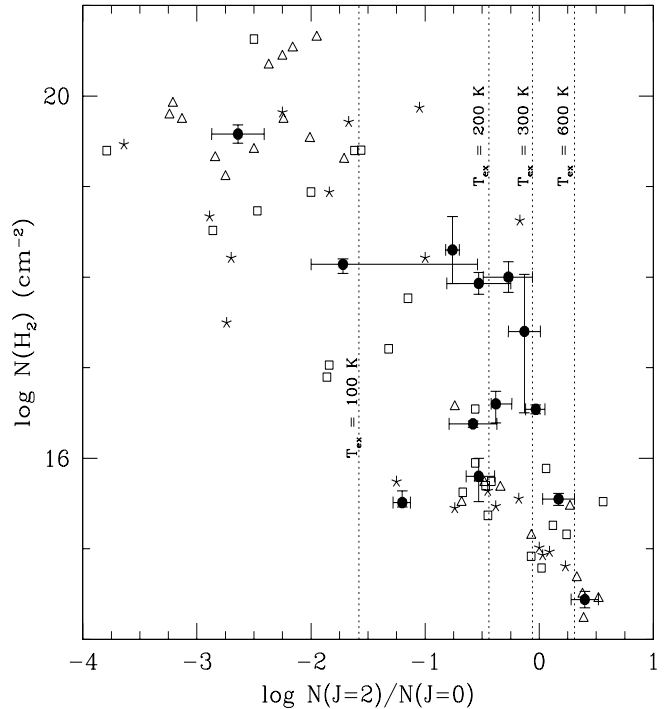


Figure 5. The $N(J=2)/N(J=0)$ ratio observed in individual DLA components (black dots) is plotted against the total molecular hydrogen column density. Other data points are from Savage et al. (1977), Spitzer, Cochran & Hirshfeld (1974) for the Galactic ISM (triangles), and Tumlinson et al. (2002) for the LMC (squares) and SMC (asterisks). The vertical dotted lines are the expected values of the column density ratio assuming the LTE for four different excitation temperatures.

equal to T_{02} (see Table 2). This is very much the case as well in most of the sightlines through the ISM and Magellanic clouds. It is well known that, due to a lower value of the Einstein coefficient of the $J = 2$ level compared to those of higher J levels, the UV and formation pumping processes can lead to enhancing the $J = 2$ level compared to the $J = 0$ level. Thus the higher values of $N(J=2)/N(J=0)$ seen in DLAs can be explained by higher pressure in the gas and/or higher radiation field.

Fig. 6 gives the $N(J=3)/N(J=1)$ ratio as a function of $N(H_2)$. The vertical dotted lines in the figure shows the expected value of the ratio for four different excitation temperatures under the LTE assumption. The measurements in DLAs are consistent with local measurements and the excitation temperature T_{03} is in the range 100–680 K (see Table 2). In Fig. 7 we plot the $N(J=3)/N(J=1)$ ratio versus the $N(J=2)/N(J=0)$ ratio. If formation and UV pumping contribute appreciably to populate the $J = 2$ and $J = 3$ levels then we expect a tight relationship between the two quantities. The dotted line in the figure gives the expected relationship between the ratios under LTE. In the case of sightlines through the Galactic ISM, the LMC or SMC, the $N(J=3)/N(J=1)$ ratio is higher than what is expected from the $N(J=2)/N(J=0)$ value under LTE (or, T_{13} is higher than T_{02}). In the case of DLAs, most of the components have T_{13} close to T_{02} (points are on top of the dotted line). Note

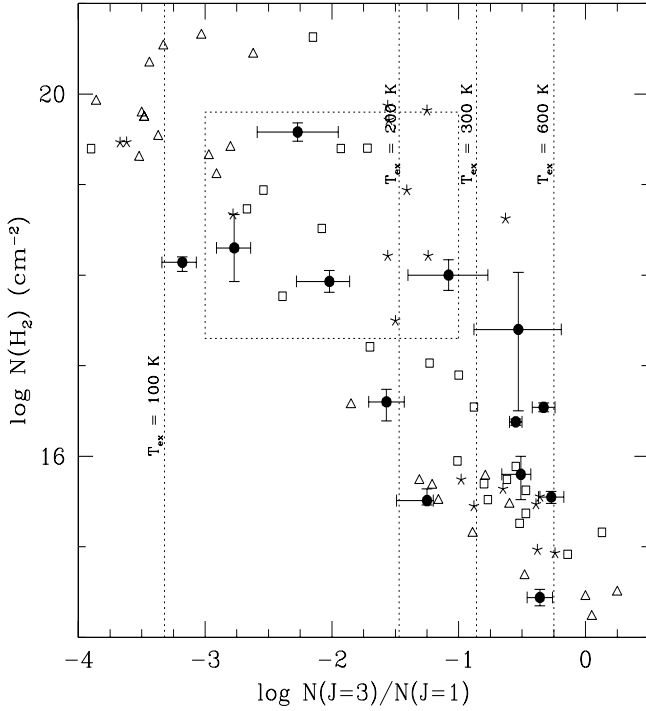


Figure 6. The $N(J=3)/N(J=1)$ ratio observed in individual DLA components (black dots) is plotted against the total molecular hydrogen column density. The box drawn with dotted lines gives the allowed range for the $z_{\text{abs}}=1.973$ components toward Q0013–004. Other data points are from Savage et al. (1977), Spitzer, Cochran & Hirshfeld (1974) for the Galactic ISM (triangles), and Tumlinson et al. (2002) for the LMC (squares) and SMC (asterisks). The vertical dotted lines are the expected values of the column density ratio assuming the LTE for four different excitation temperatures.

that these excitation temperatures are different from T_{01} . This clearly means that UV pumping and formation pumping are not negligible even for the excitation of the low J levels. The nature of the local radiation field can be probed using excitations of $J \geq 3$ levels. This is what we do in the following Section.

3.2.2 UV radiation field: High- J excitation

It is known that in the photodissociation regions (PDRs) the $J = 4$ and $J = 5$ rotational levels are populated predominantly by cascades following the formation of excited molecules and UV pumping from the low- J states. As radiative decay time-scales for these levels are very short compared to the collisional time-scales, spontaneous decay is the main deexcitation process. Among the two populating processes the UV pumping is an optical depth dependent process while the formation pumping is independent of optical depth. In an optically thick cloud, UV pumping is efficient in a thin shell surrounding the cloud. In the interior of the cloud, UV pumping becomes important only when the column density becomes very large (i.e. through absorption in the damping wings).

In Fig. 8 we plot $\log N(\text{H}_2)$ as a function of

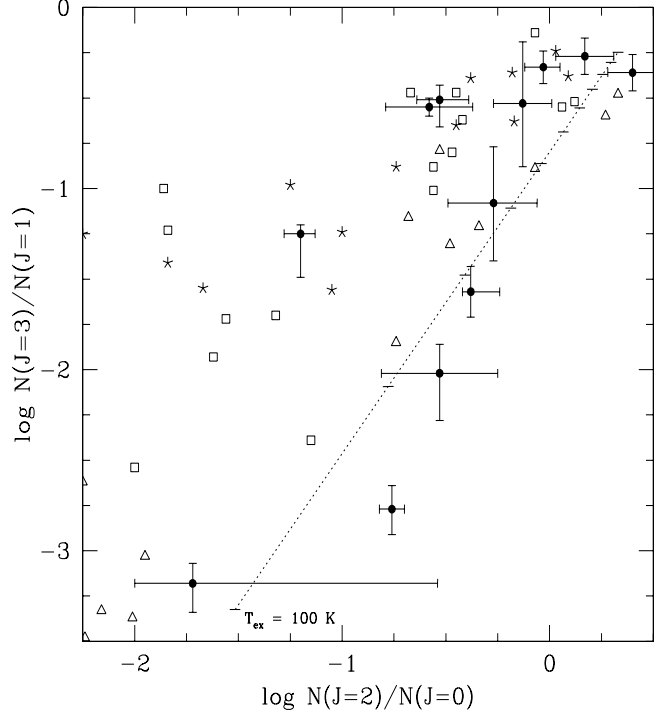


Figure 7. The $N(J=3)/N(J=1)$ vs $N(J=2)/N(J=0)$. DLA measurements are indicated by black dots. Other data points are from Savage et al. (1977), Spitzer, Cochran & Hirshfeld (1974) for the Galactic ISM (triangles), and Tumlinson et al. (2002) for the LMC (squares) and SMC (asterisks). The dotted line gives the expected relation under LTE with temperatures ranging from 100 to 600 K (horizontal tick-marks show the values for different temperatures with 50 K steps).

$\log N(J=4)/N(J=0)$ as measured in DLAs and along the ISM, LMC and SMC sightlines. As expected, a strong anti-correlation is present in the data, including DLAs. H_2 absorption lines in DLA systems have no strong overlapping wings. Therefore the high- J excitation is mostly due to photo-absorption in the systems with $\log N(\text{H}_2) \leq 16.5$ and to H_2 formation in the systems with higher column densities. Following analytic prescription by Jura (1975) we can write,

$$p_{4,0}\beta(0)n(\text{H}_2, J=0) + 0.24Rn(\text{H})n = A(4 \rightarrow 2)n(\text{H}_2, J=4) \quad (4)$$

Here, $\beta(0)$, $p_{4,0}$ are, respectively, the photo-absorption rate in the Lyman and Werner bands and the pumping efficiency from $J = 0$ to $J = 4$; $A(4 \rightarrow 2)$ is the spontaneous transition probability between $J = 4$ and $J = 2$ and R is the formation rate of H_2 . Neglecting the second term in the left hand side of Eq. 4 leads to a conservative upper limit on the UV radiation field. The vertical dashed lines in Fig. 8 represent the corresponding predicted values of the $N(J=4)/N(J=1)$ ratio for $\beta(0) = 2 \times 10^{-10} \text{s}^{-1}$ (that is, approximately the mean radiation field in the ISM) and $\beta(0) = 2 \times 10^{-9} \text{s}^{-1}$. It can be seen from Fig. 8 that for $\log N(\text{H}_2)$ less than 16.5 the $N(J=4)/N(J=0)$ ratio in DLAs is of the order of or slightly higher than that seen in the ISM of our Galaxy. Quantitatively the upper limits in most of the systems are consistent with $2 \times 10^{-10} \leq \beta(0) \leq 2 \times 10^{-9} \text{s}^{-1}$. This probably means

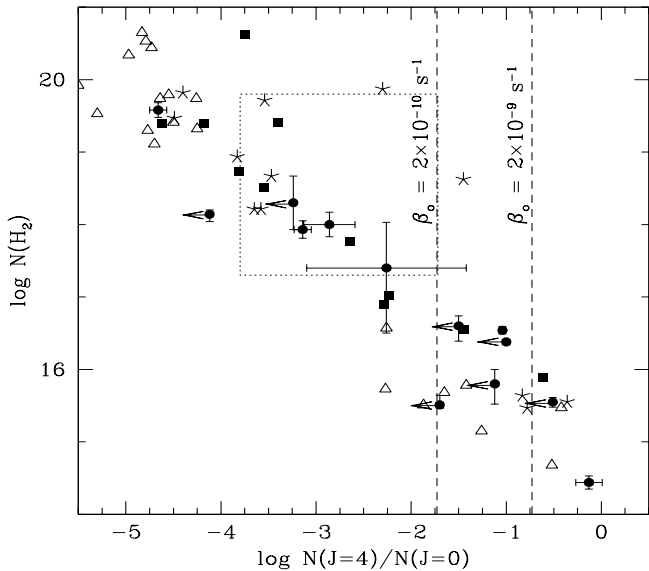


Figure 8. The $N(J=4)/N(J=0)$ ratio is plotted against the total molecular hydrogen column density. DLA measurements are indicated by black dots. Other data points are from Savage et al. (1977), Spitzer, Cochran & Hirshfeld (1974) for the Galactic ISM (triangles), and Tumlinson et al. (2002) for the LMC (squares) and SMC (asterisks). The box with dotted lines gives the allowed range for the $z_{\text{abs}}=1.973$ component toward Q0013–004. The vertical dashed lines are the expected values of the ratio for two different values of the photo-absorption rate (β_0).

the optically thin H_2 components without detectable H_2 absorption lines from the $J=4$ state arise in gas embedded in a UV field with intensity similar to (or slightly higher than) that of the mean ISM field.

There are two optically thin components in our sample ($z_{\text{abs}}=1.96822$ toward Q0013–004 and 3.02489 toward Q0347–383) that show detectable $J=4$ H_2 absorption lines. Detailed analysis of these component suggests an ambient field intensity consistent with few times the mean ISM field intensity (Petitjean et al. 2002; Levshakov et al. 2002). The same conclusion was derived by Reimers et al. (2003) for the optically thin H_2 component at $z_{\text{abs}}=1.15$ system toward HE 0515 – 4414.

The above ratio has similar values at high $\log N(H_2)$ in DLAs and in our Galaxy. This is a hint for the formation pumping in DLAs with high $N(H_2)$ being similar to the local one. There are two optically thick components (at $z_{\text{abs}}=2.59471$ toward Q0405–443 and $z_{\text{abs}}=2.08696$ toward Q1444+014) that do not show detectable absorption lines from the $J=4$ state. In the latter system the ratio $N(J=4)/N(J=0) \leq 10^{-4}$. This is much lower than the values seen in the ISM at similar total $N(H_2)$ and could be a consequence of lower H_2 formation rate in this system. High values of the radiation field intensity were inferred for some of the optically thick components when the contribution of the second term in Eq. 4 is estimated using the average metallicity and dust depletion (Ge & Bechtold 1997; Petitjean et al. 2000; Ge, Bechtold & Kulkarni 2001).

4 ANALYSIS OF CARBON ABSORPTION LINES

As the ionization potential of C I is 11.2 eV, the ionization state of Carbon is sensitive to the same photons that destroy H_2 . Therefore, C I is usually a good tracer of the physical conditions in the molecular gas (see however Srianand & Petitjean 1998). In what follows we investigate the relationship between the detectability of C I absorption line and other measurable quantities in our spectra. We derive additional constraints on the physical conditions in DLAs using C I fine-structure absorption lines.

4.1 Detectability of C I absorption lines

The results of simultaneous Voigt profile fitting to C I, C I* and C I** absorption lines in our sample are summarised in Table 3.

In the interstellar medium of our Galaxy, all clouds with $\log N(H\text{ I}) \geq 21$ have $\log N(H_2) > 19$ and $\log N(C\text{ I}) > 14$ (Jenkins & Shaya 1979; Jenkins, Jura & Loewenstein 1983). In our sample, C I absorption lines are detected in most of the DLAs that show H_2 absorption lines (see also Ge & Bechtold 1999). There are three exceptions: the components at $z_{\text{abs}}=2.59471$ and 2.59486 toward Q0405–443 and at $z_{\text{abs}}=2.81100$ toward PKS 0528–250. These C I non-detections are surprising as the H_2 absorption lines from these components are optically thick so that C I is expected to be conspicuous.

Usually, DLAs in which no H_2 is detected through the whole profile do not show any detectable C I absorption line (with a typical upper limit of 10^{12} cm^{-2}). The only exception is the high-metallicity sub-DLA at $z_{\text{abs}}=2.139$ toward Tol 1037–270 (see Srianand & Petitjean 2001). On the contrary, in DLAs where H_2 is detected, some components show detectable C I absorption line without detectable molecular absorption ($N(H_2) \leq 10^{14}\text{ cm}^{-2}$). This is the case in Q0013–004 (Petitjean et al. 2002) and Q0551–366 (Ledoux et al. 2002).

Note that C I is also detected at $z_{\text{abs}}=2.28749$ toward Q2332–094 but the presence of H_2 molecules can not be probed in this system due to the presence of an intervening Lyman limit system. The sub-DLA at $z=1.15$ toward HE 0515–4414 shows C I and H_2 absorption lines (Quast et al. 2002; Reimers et al. 2003). C I absorption lines have also been detected at $z_{\text{abs}}=1.776$ system toward Q1331+170 (Chaffee et al. 1988). Presence of H_2 in this system is recently reported (Cui et al., 2004).

4.1.1 Dependence on H_2 column density

Jenkins & Shaya (1979) found $N(C\text{ I})$ does not scale linearly with either of $N(H\text{ I})$, $N(H_2)$ or $N(H_{\text{total}})$ in the Galactic ISM. They explained this behavior as a result of strong differences in the response of C I, H I and H_2 to physical conditions (electron density, temperature etc...), coupled with marked variations of these conditions from one cloud to the other. In Fig. 9, we plot the C I column density as a function of H_2 column density in individual components. Among the systems that show H_2 absorption lines (filled circles with error-bars) there is no clear trend between $N(H_2)$ and $N(C\text{ I})$ even though the presence of C I absorption lines usually indicate the presence of H_2 (see discussion above).

Table 3. DLA systems with detected C I absorption lines in the sample of Ledoux et al. (2003)

Quasar/ log N(H I)	z_{abs}	$\log N(\text{H}_2)$	$\log N(\text{C I})$	$\log N(\text{C I}^*)$	$\log N(\text{C I}^{**})$	$b(\text{km s}^{-1})$	$T_{\text{CMB}}(\text{K})$	$n_{\text{H}}(\text{cm}^{-3})$	$P/k(\text{cm}^{-3} \text{K})$
Q 0013–004	1.96679	^a 16.38 ^{+0.03} _{–0.04}	13.06 ± 0.04	12.72 ± 0.05	3.1±0.6	< 13.8	20 – 70	2000–7000
20.83(0.05)	1.96691	12.86 ± 0.03	12.55 ± 0.07	3.0±0.2	< 14.5	20 – 80	2000–8000
	1.96706	12.31 ± 0.07	12.26 ± 0.11	4.93±1.44
	1.96822	16.54 ^{+0.05} _{–0.05}	13.04 ± 0.01	13.10 ± 0.01	12.77 ± 0.02	4.3±0.2	< 20.0	170 – 200	11730 – 12400
	1.97280	^b 17.48–19.78	13.08 ± 0.01	12.77 ± 0.03	6.0±0.3	< 13.0	40 – 60	4000–6000
	1.97296	13.44 ± 0.01	13.20 ± 0.01	12.53 ± 0.04	6.2±0.2	< 13.5	50 – 65	5000 – 6500
	1.97316	12.66 ± 0.03	12.33 ± 0.10	7.0±0.8	< 15.0	10 – 85	1000–8500
	1.97365	^c 17.30–19.60	12.32 ± 0.05	< 12.11	5.7±0.4	< 15.0	< 85	< 8500
	1.97382	12.40 ± 0.04	12.04 ± 0.13	4.5±0.4	< 15.5	< 95	< 9500
	1.97399	11.91 ± 0.13	7.3±1.0
	1.97417	11.49 ± 0.25	0.4±0.3
	1.96737	< 14.0	12.91 ± 0.03	12.77 ± 0.06	14.4±1.1	< 17.5	40 – 135	4000–13500
	1.96763	< 14.0	12.85 ± 0.05	12.68 ± 0.09	27.1±3.4	< 19.3	20 – 180	2000–18000
	1.97109	< 14.0	12.28 ± 0.03	< 12.11	10.0±0.9	< 21.0	< 2000	< 20000
	1.97144	< 14.0	12.96 ± 0.03	12.91 ± 0.03	13.4±0.9	< 18.5	65 – 160	6500–16000
Q 0347–383	3.02485	14.55 ^{+0.09} _{–0.09}	11.73 ± 0.26	< 11.50	< 11.75	4.9 ± 0.3	< 17.0	< 48	< 4800
20.73(0.05)									
Q 0405–443	2.59474	18.14 ^{+0.07} _{–0.12}	< 12.23
21.05(0.10)	2.59485	15.51 ^{+0.15} _{–0.07}	< 11.90
Q 0528–250	2.81100	17.93 ^{+0.14} _{–0.20}	< 12.00
21.35(0.10)	2.81112	17.90 ^{+0.11} _{–0.14}	12.36 ± 0.10	12.30 ± 0.10	0.6±0.1	< 17.0	25 – 270	3250 – 17000
Q 0551–366	1.96152	< 14.0	12.69 ± 0.07	< 12.18	< 11.94	4.3 ± 1.4	< 10.5	< 17	< 1700
20.70(0.10)	1.96168	15.80 ^{+0.40} _{–0.14}	12.64 ± 0.07	12.84 ± 0.07	< 12.16	2.1 ± 0.7	< 22.3	170 – 185	12950 – 14280
	1.96180	< 14.0	12.42 ± 0.13	< 12.18	< 11.94	3.9 ± 2.3	< 12.9	< 56	< 5600
	1.96214	17.40 ^{+0.65} _{–0.93}	12.66 ± 0.12	12.69 ± 0.11	12.11 ± 0.34	2.1 ± 0.8	< 18.7	55 – 390	8250 – 30400
	1.96221	15.58 ^{+0.03} _{–0.12}	13.16 ± 0.06	12.98 ± 0.09	12.26 ± 0.36	12.8 ± 1.7	< 14.5	30 – 150	3840 – 15150
	1.96268	< 14.0	12.63 ± 0.08	< 12.18	< 11.94	4.0 ± 1.8	< 10.0	< 25	< 2500
Q 1037–270	2.13900	< 14.0	12.51 ± 0.02	< 12.48	15.5±0.6	< 16.4	< 105	< 10500
19.70(0.05)	2.13940	< 14.0	12.48 ± 0.02	< 12.30	4.5±1.2	< 13.2	< 65	< 6500
Q 1232+082	2.33771	19.57 ^{+0.12} _{–0.12}	13.86 ± 0.22	13.43 ± 0.07	12.63 ± 0.22	1.7 ± 0.1	< 14	40 – 60	2320 – 5280
20.90(0.08)									
Q 1444+014	2.08679	16.60 ^{+0.28} _{–0.11}	12.67 ± 0.09	12.52 ± 0.14	11.6 ± 2.8	< 18.5	20 – 110	6560 – 27280
20.25(0.07)	2.08692	18.15 ^{+0.15} _{–0.15}	12.82 ± 0.11	12.42 ± 0.12	1.1 ± 0.3	< 14.0	4 – 54	824 – 10260
Q 2332–094	2.28749	13.33 ± 0.03	13.14 ± 0.03	12.34 ± 0.11	3.8 ± 0.3	< 14.6	45 – 75	4500 – 7500
20.25(0.07)									

^a total H₂ column density in three components at $z_{\text{abs}}=1.96679, 1.96691$ and 1.96706 is quoted.

^b total H₂ column density in three components at $z_{\text{abs}}=1.97280, 1.97296$ and 1.97316 .

^c total H₂ column density in four components at $z_{\text{abs}}=1.97365, 1.97382, 1.97399$ and 1.97417 is quoted.

4.1.2 The Carbon ionization state

The probability of detecting C I is expected to be higher in systems with higher $N(\text{H I})$ and/or metallicity. Ideally, we would like therefore to know $N(\text{H I})$ for each individual C I components. This is not possible as all components are definitely blended in one strong H I DLA absorption line. Estimation of $N(\text{H I})$ is possible when the H₂ component is well separated from the rest of the components (as in $z_{\text{abs}}=1.96822$ toward Q 0013–004) or when 21 cm observations are available (as in the case of H₂ components toward Q 0528–250). Note that the presence of very strong C I absorption line in the component at $z_{\text{abs}}=1.96822$ toward Q 0013–004 (that has $\log N(\text{H I}) \leq 19.4$) is mainly due to high metallicity (Petitjean et al. 2002). Whereas the absence of C I in the component at $z_{\text{abs}}=2.81100$ and the weakness of C I line of the component at $z_{\text{abs}}=2.81112$ component toward Q 0528–250 are probably due to excess radiation field from the QSO.

The ionization state of Carbon is difficult to determine as the C II λ 1334 absorption line is usually highly saturated. We can however partly overcome this difficulty assuming that conditions are fairly homogeneous in the DLA system. Under the assumptions that the enrichment of Carbon follows that of α -elements and that the relative depletion between Sulfur and Carbon is negligible, we can use the well determined $N(\text{S II})$ as an indicator of $N(\text{C II})$ (see Fig. 10). In the sun, the Carbon abundance is 1.28 dex higher than that of Sulfur and typical depletion of Carbon relative to Sulfur in the Cold ISM is 0.4 dex (see Table 5 of Welty et

al. 1999). The two dotted lines in Fig. 10 give the expected correlation for $\log N(\text{C I})/N(\text{C II}) = -3$ (lower line) and -2 (upper line) respectively, when relative solar abundances are used and it is assumed that there is no depletion of Carbon relative to Sulfur. The short-dashed lines give the same correlations when a depletion of Carbon relative to Sulfur of 0.4 dex is further assumed. If the absorbing gas originates from the CNM then $\log N(\text{C I})/N(\text{C II})$ is expected to be more than -3 (see Fig. 3 of Liszt 2002). Therefore, within uncertainties due to depletion, it is apparent from Fig. 10 that the DLA components with C I detections have a ionization state consistent with them originating from the CNM.

It is interesting to note that the distribution of $N(\text{S II})$ is somewhat similar for components with both H₂ and C I absorption lines (filled circles), and for components with C I but no H₂ absorption lines (open circles). However C I column densities are typically lower in the components without H₂ suggesting, as expected, that when H₂ is seen, the C I/C II ratio is larger.

Most of the upper limits on C I are consistent with $N(\text{C I})/N(\text{C II}) \leq -3$ (see Fig. 10). This can mean either that the relative depletion of Carbon compared to Sulfur is larger than 0.4 dex in the CNM, which is unlikely, or that most of the DLA systems originate from the warm neutral medium (WNM) or warm ionized medium (WIM) where the above ratio can be as low as 10^{-4} .

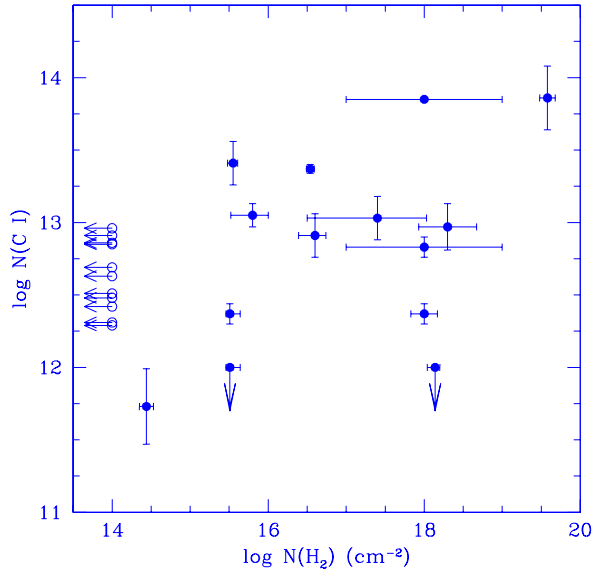


Figure 9. The column density of C I measured in individual components of DLAs is plotted as a function of $N(H_2)$. The filled circles with error-bars are points from the components that show detectable H_2 absorption lines. The open circles are the measurements from components that show C I without detectable H_2 .

4.1.3 The effect of dust

In Fig. 11 we plot $\log N(C I)$ against the depletion factor defined as $\log(N(Fe II)/N(X II)) - [Fe/X]_{\odot}$ with either $X = Zn, S$ or Si . C I absorption line is not detected in systems with low depletion factors (i.e., $[Fe/Zn]$ less than -0.5 dex) whereas components with higher depletion factors readily show detectable C I absorption lines. This trend is not surprising as there is a 4σ correlation between the depletion factor and the metallicity of the gas in our sample (see Figure 12 of Ledoux et al. 2003). Depletion factors lower than 0.5 dex are usually seen in systems with $[Zn/H] \leq -1$. High depletion factor in high metallicity gas implies high dust content and hence high dust optical depth to the UV radiation. The absence of C I in components with low dust depletion is a combination of low metallicity and low dust optical depth to the UV radiation. It is worth remembering that similar relation exists between the detectability of H_2 and depletion (Fig. 14 of Ledoux et al. 2003).

4.2 C I fine-structure excitation

In most of the DLAs with C I detections we also detect absorption lines from the excited fine-structure levels. It is therefore possible to use the relative populations of the C I ground state levels to discuss the particle density, the ambient UV radiation field and the temperature of the cosmic-microwave background radiation (see Bahcall et al., 1973; Meyer et al., 1986; Songaila et al. 1994; Ge, Bechtold & Black, 1997; Roth & Bauer, 1999; Srianand et al. 2000; Silva & Viegas, 2002; Quast et al. 2002). In the Galactic ISM, fine-structure excitation of C I has been used to study the distribution of thermal pressure (see Jenkins & Tripp 2001). In Fig. 12 we plot the ratio $N(C I^*)/N(C I)$ as a func-

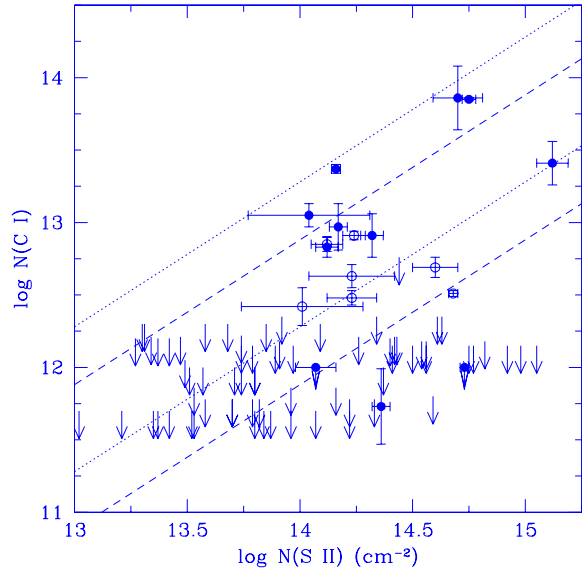


Figure 10. The C I column density measured in individual components of DLAs is plotted as a function of the S II column density. The filled circles with error-bars are points from components that show detectable H_2 absorption lines. The open circles are the measurements from components that show C I but no detectable H_2 . The arrows are the upper limits from systems where there is no H_2 and/or C I absorption lines. The two dotted lines give the expected correlation for $\log N(C I)/N(C II) = -3$ (lower line) and -2 (upper line) respectively, when solar relative abundances are used and it is assumed that there is no depletion of Carbon relative to Sulfur. The short-dashed lines give the same correlations when a depletion of Carbon relative to Sulfur of 0.4 dex is further assumed. The C I detections are consistent with what one expects in the case of the CNM.

tion of $N(C I)$. It is clear that the C I column densities in DLAs (filled circles with error-bars) are at least an order of magnitude less than that measured in the ISM (stars). This is probably a consequence of lower metallicities and/or low $H I$ content in DLA components. The important point is that the $N(C I^*)/N(C I)$ ratio measured in DLAs is remarkably larger than in the Galaxy. However, while comparing the ISM and DLAs, it is important to remember that most of the sightlines used by Jenkins & Tripp (2001) have H_2 fraction orders of magnitude higher than what we measure in DLA components. As H_2 collisions are less efficient in populating the excited fine-structure state of C I we expect that for a given total hydrogen density (and a given kinetic temperature) $N(C I^*)/N(C I)$ be higher in DLAs.

The horizontal dotted line in Fig. 12 indicates the expected value of the ratio if it is assumed that the excitation is due to the CMBR only with a temperature $T_{CMBR} = 8.1$ K as expected at $z = 2$, the typical redshift of our sample. It is clear that the CMBR field expected from the Big-Bang is not sufficient to explain the observed ratios and an extra contribution is required from collisional processes and/or the UV flux.

Collisions with H, He, e, p and H_2 can populate the excited state of C I. As $H I$ is the dominant form of hydrogen in the gas, the contribution to the fine-structure excitation by H_2 collisions can be neglected. The electron

Table 4. Physical conditions in systems in which C I is detected

QSO	z_{abs}	$\log N(\text{S II})$	$\log N(\text{C II}^*)$	$n_e \text{ (cm}^{-3}\text{)}^a$	$n_{\text{H}} \text{ (cm}^{-3}\text{)}$
Q 0013 – 004	1.96679 ⁺	14.27 ± 0.05	2.7 10 ⁻²
	1.96822 ⁺	14.16 ± 0.02	4.9 10 ⁻²
	1.97280 ⁺	14.15 ± 0.06	3.8 10 ⁻²
	1.97296 ⁺	14.75 ± 0.03	2.3 10 ⁻²
	1.97316 ⁺	13.91 ± 0.05	2.4 10 ⁻²
	1.97365 ⁺	13.86 ± 0.08	1.5 10 ⁻²
	1.97382 ⁺	14.12 ± 0.05	8.0 10 ⁻³
	1.97399 ⁺	13.55 ± 0.16	6.9 10 ⁻³
	1.96737	14.24 ± 0.05	2.4 10 ⁻²
	1.96763	14.12 ± 0.07	2.7 10 ⁻²
	1.97109	14.77 ± 0.01	1.0 10 ⁻³
	1.97144	14.08 ± 0.03	4.3 10 ⁻²
	Q 0347 – 383	3.02463	14.50 ± 0.03	< 13.00	< 5.0 10 ⁻⁴
3.02485 ⁺		14.36 ± 0.04	13.55 ± 0.23	2.3 10 ⁻³	4.4 – 41.9
3.02501		13.51 ± 0.12	< 12.72	< 4.9 10 ⁻³	< 32
Q 0405 – 443	2.59440	13.91 ± 0.04	< 12.41	< 3.7 10 ⁻³	< 6.3
	2.59464	14.72 ± 0.02	13.09 ± 0.10	< 5.7 10 ⁻⁴	3.0 – 7.5
	2.59474 ⁺	14.07 ± 0.09	13.20 ± 0.20	< 2.5 10 ⁻³	7.7 – 57.3
	2.59485 ⁺	14.73 ± 0.02	13.25 ± 0.08	< 5.6 10 ⁻⁴	4.5 – 10.3
Q 0551 – 366	1.96152	14.60 ± 0.10	< 12.00	3.7 10 ⁻³	< 0.5
	1.96168 ⁺	14.01 ± 0.27	13.93 ± 0.09	3.2 10 ⁻²	123.0 – 331.8
	1.96180	14.23 ± 0.19	< 12.00	4.6 10 ⁻³	< 1.2
	1.96214 ⁺	<i>Blended</i>	12.58 ± 0.09
	1.96221 ⁺	<i>Blended</i>	13.36 ± 0.07
	1.96268	14.63 ± 0.11	12.98 ± 0.08	3.0 10 ⁻³	2.4 – 9.6
Q 1037 – 270	2.13900	14.68 ± 0.02	< 13.50	2.0 10 ⁻³	< 13.2
	2.13940	14.23 ± 0.11	13.31 ± 0.01	5.3 10 ⁻³	< 14.2
Q 1232 + 082	2.33771 ⁺	15.24 ± 0.11 ^b	< 14.00	< 7.0 10 ⁻²	< 48
Q 1444 + 014	2.08679 ⁺	14.32 ± 0.05	13.12 ± 0.08	1.1 10 ⁻²	0.9 – 9.9
	2.08692 ⁺	14.17 ± 0.06	12.78 ± 0.20	1.9 10 ⁻²	< 13.0

A label “+” indicates a component in which H₂ is detected

^a Derived from the Carbon ionization equilibrium

^b column density of Si II is given.

and proton densities are expected to be very small, at least smaller by two orders of magnitude than the hydrogen density, and their contribution is also negligible (Keenan et al. 1986). The He I collisional rates are much less than that of H I and the He I/H I ratio is small which makes collisions with He I unimportant (see Fig. 1 of Silva & Viegas 2002). Thus in our analysis of the C I excitation we consider only collisions by neutral hydrogen. The rates are taken from Launay & Roueff (1977). The spontaneous decay rates are $A_{10} = 7.93 \times 10^{-8} \text{ s}^{-1}$ and $A_{21} = 2.68 \times 10^{-7} \text{ s}^{-1}$ (Bahcall & Wolf 1968). The corresponding CMBR excitation rate is derived from these values. The UV pumping rate in the cloud depends on the nature and strength of the UV radiation field. We assume that the UV intensity is the same as in the ISM of our Galaxy as suggested by the high- J excitation of H₂.

The dashed lines in Fig. 12 give the expected ratio for, $T_{\text{CMBR}} = 8 \text{ K}$, a UV radiation field like in the Galaxy (with an excitation rate of $\Gamma_{01} = 7.55 \times 10^{-10} \text{ s}^{-1}$), hydrogen density in the range $n_{\text{H}} = 20\text{--}250 \text{ cm}^{-3}$, versus the kinetic temperature, T_{kin} , in the range 80 – 200 K (consistent with T_{01} measured in DLAs). It can be seen that a typical density range consistent with most of the observed point is, $20 \leq n_{\text{H}}(\text{cm}^{-3}) \leq 150$. The density (n_{H}) and pressure (p/K) derived for individual components are summarized in column 9 and 10 respectively in Table. 3. Here, we assume

$T_{\text{CMBR}} = 2.7 \times (1 + z_{\text{abs}})$ and $T = T_{01}$ in the case of H₂ detection and $T = 100 \text{ K}$ otherwise. The derived pressure range in DLA components are higher than that typically measured in the galactic ISM (see Jenkins & Tripp 2001) and consistent with what is expected in a the cold neutral medium (CNM) with lower metallicity ($Z \sim 0.1 Z_{\odot}$) and dust depletion (see Wolfire et al. (1995, 2001), Wolfe et al., (2003a, b) Srianand et al. 2005). Interestingly the derived density range in most of the components is close to the critical density for thermalising the H₂ $N(J=2)/N(J=0)$ ratio (see Fig. 4).

5 CARBON IONIZATION STATE

In the ISM, when hydrogen is neutral, most of the carbon is in the form of C II so that we can use the C I/C II ratio to derive the physical conditions in the gas. As already mentioned, the C II absorption features are always badly saturated and we rely on the realistic assumption that C II in the neutral phase can be traced by S II and/or Si II so that we can use the weak lines of these species to derive the C II column densities in the components of interest.

Assuming photoionization equilibrium between C I and C II and using the atomic data from Shull & Van Steenberg (1982) and Péquignot et al. (1991), we can write,

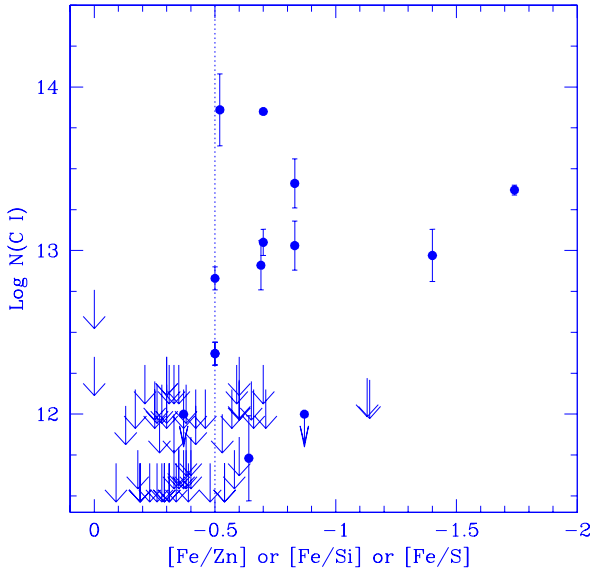


Figure 11. The column density of C I measured in individual components is plotted as a function of the metal depletion factor computed using [Fe/Zn] or [Fe/S] or [Fe/Si]. It is apparent from this figure that C I absorption line is usually detected in components with high depletion factors.

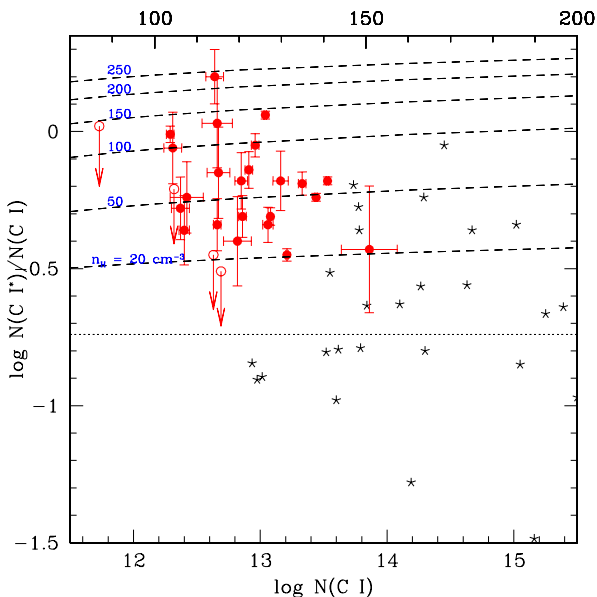


Figure 12. The ratio $N(C I^*)/N(C I)$ is plotted on a logarithmic scale as a function of $N(C I)$. The points with error bars are our measurements in individual DLA components. The stars are data measurements in the ISM of the Galaxy drawn from Jenkins & Tripp (2001) and Jenkins, Jura & Loewenstein (1983). The horizontal dotted line gives the expected value of the ratio if it is assumed that C I is excited by the CMBR only with $T_{\text{CMBR}} = 8.1$ K as expected at $z = 2$. The short dashed lines give the expected ratio for different n_H as a function of temperature (top portion of the x-axis).

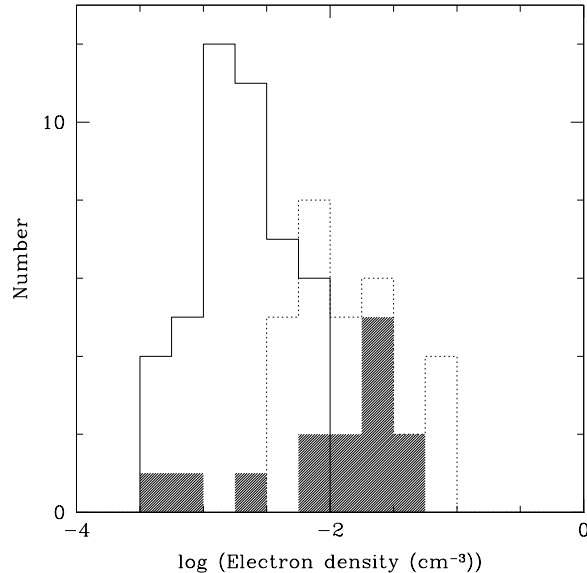


Figure 13. Histogram of the electron density derived using Eq. 5 for $T = 100$ K. The shaded histogram is based on systems that show detectable C I absorption lines. The histograms with continuous and dotted lines are upper limits on the electron density for, respectively, systems with $\log N(C II)$ greater and less than 15. We use the C I photoionization rate given for the Galactic UV field by Péquignot & Aldrovandi (1986).

$$\frac{n_e}{\Gamma} = 4.35 \times 10^{11} \frac{N(C I)}{N(C II)} \left(\frac{T}{10^4} \right)^{0.64} \quad (5)$$

Here, Γ is the photoionization rate for C I. In the local ISM, $\Gamma_{\text{gal}} \simeq 2 - 3.3 \times 10^{-10} \text{ s}^{-1}$ (Péquignot & Aldrovandi 1986). Here, we neglect the ion-molecular interaction and charge exchange reactions that may produce C I. Thus n_e/Γ can be constrained once the temperature of the gas is known. Application of Eq. 5 to the cold Galactic ISM (with $T = 100$ K) has resulted in $n_e \simeq 0.14 \pm 0.07 \text{ cm}^{-3}$ (Welty et al. 2002 and references therein). In the stable CNM considered by Wolfire et al. (1995) the electron density is expected to be in the range $0.01 \leq n_e (\text{cm}^{-3}) \leq 0.02$ for $Z = 0.1 Z_{\odot}$ and dust abundance one tenth of the Galactic ISM.

5.1 Systems with C I detections

First we concentrate on the systems with C I detections. We estimate the electron density assuming a UV field similar to the Galactic mean field (i.e., $\Gamma_{\text{gal}} = 2.5 \times 10^{-10} \text{ s}^{-1}$), $T = T_{01}$ for the H_2 components and $T = 100$ K otherwise. Individual values of n_e derived for these systems are given in Table 4. The electron density is in the range $0.7 \times 10^{-2} \leq n_e (\text{cm}^{-3}) \leq 4.9 \times 10^{-2}$. Together with n_H given in Table 3, this suggests that $n_e/n_H \leq 10^{-3}$ for most of the systems. Therefore, the ionization state of the gas with H_2 and C I is similar to that in the CNM in a moderate radiation field.

5.2 Systems without H_2 and C I

In the case of systems in which neither H_2 nor C I are detected, we assume $T = 100$ K and $\Gamma_{\text{gal}} = 2.5 \times 10^{-10} \text{ s}^{-1}$ and obtain upper limits on the electron density. The results

are plotted in Fig. 13. We notice that the inferred electron densities are much smaller than in systems in which C I (and H₂) are detected. The difference is even larger if we use only the systems with $\log N(\text{C II}) \leq 15$. For this gas the inferred electron densities are less than 10^{-2} cm^{-3} (with a median of 10^{-3} cm^{-3}). This may indicate that the absorption originates from warm neutral medium (say $T = 8000 \text{ K}$). If the average radiation field in DLAs is similar to that in the Galactic ISM then the absence of C I in most of the DLAs could just be a consequence of lower densities (and/or higher T) in these systems. One can derive an independent estimate of the particle density using the excitation of C II fine structure levels. This is what we do in the following Section.

6 EXCITED FINE-STRUCTURE LINE OF C II

6.1 Method to derive physical parameters

Under LTE, the column density ratio $N(\text{C II}^*)/N(\text{C II})$, can be written as,

$$\frac{N(\text{C II}^*)}{N(\text{C II})} = \frac{Q_{12}(\text{e}) n_{\text{e}} + Q_{12}(\text{H}) n_{\text{H}} + \Gamma_{12}(\text{CMB})}{A_{21}} \quad (6)$$

where, $Q_{12}(\text{e}) = 7.8 \times 10^{-6} \exp[-91.27/T] T^{-0.5} \text{ cm}^{-3} \text{ s}^{-1}$ and $Q_{12}(\text{H}) = 1.3 \times 10^{-9} \exp[-91.27/T] \text{ cm}^{-3} \text{ s}^{-1}$ are the collisional excitation rates per unit volume for electrons and hydrogen atoms (Bahcall & Wolf 1968) with T being the kinetic temperature of the gas. The Einstein's coefficient is $A_{21} = 2.291 \times 10^{-6} \text{ s}^{-1}$. The CMB pumping rate, $\Gamma_{12}(\text{CMB})$, equals $6.6 \times 10^{-11} \text{ s}^{-1}$ and $1.1 \times 10^{-9} \text{ s}^{-1}$ for, respectively, redshifts 2 and 3 (Silva & Viegas 2002). For a given temperature, the collisional excitation rate for electrons is orders of magnitude larger than that for hydrogen atoms. For example, when $T = 1000 \text{ K}$, whenever $n_{\text{e}}/n_{\text{H}}$ is larger than 5×10^{-3} , collisions with electrons is the dominant process. UV pumping is an additional possible excitation mechanism. For the mean radiation field in our Galaxy, the UV pumping rate is $9.3 \times 10^{-11} \text{ s}^{-1}$ (Silva & Viegas 2002). This is similar to or slightly lower than the CMB pumping rate for the range of redshift we consider in this study.

We compute the expected value of $\log N(\text{C II}^*)/N(\text{C II})$ ratio under different situations and in particular the WNM and CNM solutions given in Table 3 of Wolfire et al. (1995). Note that if CMBR pumping alone is responsible for the excitation, the expected ratios are -4.54 and -3.31 for, respectively, $z_{\text{abs}} = 2$ and 3. For the standard ISM (with stable pressure in the range $990\text{--}3600 \text{ cm}^{-3} \text{ K}$), we derive $-2.62 \leq \log N(\text{C II}^*)/N(\text{C II}) \leq -2.20$ for the CNM and $-3.65 \leq \log N(\text{C II}^*)/N(\text{C II}) \leq -3.17$ for the WNM. As the DLA gas has low metallicity and low dust content, the expected pressure should be higher in the two DLA phases (see Liszt 2002 and Wolfe et al. 2003). If we assume $Z = 0.1Z_{\odot}$ and dust to gas ratio one tenth of the ISM value (which is typical of DLAs) then we expect $-2.26 \leq \log N(\text{C II}^*)/N(\text{C II}) \leq -2.08$ for the CNM and $-3.39 \leq \log N(\text{C II}^*)/N(\text{C II}) \leq -2.70$ for the WNM in DLAs. Thus if DLAs originate from H I gas in a two-phase equilibrium, we expect the CMBR pumping to be sub-dominant compared to collisional excitation. In fact if the gas is completely neutral then from Eqs. (5) and (6) we

derive,

$$\begin{aligned} n_{\text{H}} &= \frac{A_{21}N(\text{C II}^*)}{\sigma_{\text{H}}N(\text{C II})} - \frac{\sigma_{\text{e}}n_{\text{e}}}{\sigma_{\text{H}}} \\ &= \frac{A_{21}N(\text{C II}^*)}{\sigma_{\text{H}}N(\text{C II})} - \frac{\sigma_{\text{e}}N(\text{C I})\Gamma}{\sigma_{\text{H}}\alpha_{\text{r}}N(\text{C II})}. \end{aligned} \quad (7)$$

This gives an independent estimate of n_{H} which, by comparison with the estimate derived from the C I excitation, can lead to constraints on the radiation field. However, the ionization fraction (i.e $n_{\text{e}}/n_{\text{H}}$) and the temperature of the neutral absorbing gas must be accurately determined before densities can be derived using the $N(\text{C II}^*)/N(\text{C II})$ ratio. Indeed, the fact that, in DLAs, the Al III absorption profile is very similar to that of neutral or singly ionized species has been used as evidence for the presence of ionized gas being mixed with the neutral gas in DLAs (Lu et al. 1996; Prochaska & Wolfe 1999; Howk & Sembach 1999; Wolfe & Prochaska 2000; Vladilo et al. 2001; Izotov et al. 2001). In the ionized gas (i) n_{e} as well as T will be higher than what is expected in the warm or cold neutral gas and (ii) $N(\text{Si II})$ will under-predict $N(\text{C II})$ as the ionization corrections are different for the two species (see Fig. 1 of Izotov et al. 2001). Neglecting the presence of ionized gas can artificially enhance the derived n_{H} values.

6.2 Frequency of C II* detection

In our sample, all the systems that show H₂ also show detectable C II* absorption line. The details of the fits to the C II* absorption line for these systems are summarized in Table 5 and shown in Fig. 14. The components toward Q0013 – 004 and Q0528 – 250 are badly blended and it is therefore not possible to fit $N(\text{C II}^*)$. We detect C II* in seven out of the 21 DLAs that do not show H₂ absorption lines. If we also include the 8 DLAs that show H₂, about 50% (15 out of 29) of the DLAs in our sample show detectable C II* absorption line which is consistent with the finding by Wolfe et al. (2003).

In Fig. 15 we plot the average (over the whole profile) $N(\text{C II}^*)/N(\text{C II})$ ratio measured in DLAs in our sample together with the measurements by Wolfe et al. (2003a, 2003b) against the total H I column density and the silicon metallicity. Here we use the total column density summed over all the components. $N(\text{C II})$ is computed from $N(\text{Si II})$ assuming solar abundance ratio without any ionization correction. From the upper panel in Fig. 15 it can be seen that C II* is detected in all the systems with $\log N(\text{H I}) \geq 21.0$. Interestingly no such relationship exists between C I (or H₂) and H I. Most the systems with $\log N(\text{H I}) \geq 21.0$ have $N(\text{C II}^*)/N(\text{C II})$ consistent with what is expected in CNM. On the contrary, the measured values of $N(\text{C II}^*)/N(\text{C II})$ in systems with lower $N(\text{H I})$ spread over more than an order of magnitude covering the expected ranges for WNM and CNM.

From the bottom panel, it can be seen that C II* is frequently detected in gas with high metallicity as already noticed by Wolfe et al. (2003a). Most of the systems that show C II* absorption line with lower $N(\text{H I})$ do have statistically higher metallicity. In the whole sample the number of systems with C II* detections that are consistent with CNM and WNM are approximately equal. Most of the upper limits on the ratio, measured in the metallicity range

Table 5. Results of Voigt profile fits to DLAs that do not show detectable H_2 absorption lines

Quasar	$\log N(\text{H I})$	Z/Z_\odot	z_{abs}	$\log N(\text{C I})$	$\log N(\text{Si II})$	$\log N(\text{S II})$	[Fe/X]	$\log N(\text{C II}^+)$	$b(\text{km s}^{-1})$	X
Q 0000–263	21.40(0.08)	–2.06(0.09)	3.39013	15.06(0.02)	14.70(0.03)	+0.03(0.06)	10.0(0.3)	Zn
Q 0010–002	20.95(0.10)	–1.43(0.11)	2.02471	< 12.15	14.90(0.05)	14.50(0.05)	+0.18(0.08)	< 13.40	5.5(0.4)	Zn
			2.02484	< 12.15	15.09(0.03)	14.77(0.03)	+0.15(0.07)	< 13.40	8.4(0.5)	Zn
Q 0058–292	21.10(0.10)	–1.53(0.10)	2.67123	< 12.35	14.87(0.07)	14.61(0.03)	–0.69(0.05)	12.82(0.04)	8.7(0.7)	Zn
			2.67142	< 12.35	14.98(0.05)	14.63(0.03)	–0.13(0.04)	12.79(0.04)	8.2(0.2)	Zn
Q 0102–190	21.00(0.08)	–1.90(0.09)	2.36958	< 12.30	13.93(0.04)	–0.16(0.06)	< 12.92 ⁺	2.0(0.2)	S
			2.36966	< 12.30	14.06(0.03)	–0.17(0.04)	< 13.02 ⁺	3.5(0.2)	S
Q 0112–306	20.50(0.08)	–2.43(0.09)	2.41844	< 12.32	13.31(0.02)	< 14.14	–0.15(0.04)	< 13.20	3.5(0.2)	Si
			2.41861	< 12.32	13.33(0.02)	< 14.14	–0.33(0.09)	< 13.20	6.9(0.4)	Si
	20.30(0.10)	–0.50(0.15)	2.41869	< 12.32	< 12.44	< 14.14	> +0.33	< 13.20	5.6(1.1)	Si
			2.70111	< 12.20	< 14.20	> –0.61	< 13.20	7.2(0.8)	Si
			2.70163	< 12.20	14.75(0.05)	–0.48(0.06)	< 13.00	27.4(2.2)	Si
			2.70217	< 12.20	14.76(0.10)	–0.66(0.15)	< 13.00	14.9(3.1)	Si
			2.70233	< 12.20	14.29(0.18)	–0.21(0.22)	12.60 ± 0.08	3.6(1.2)	Si
			2.70257	< 12.20	14.58(0.05)	–0.47(0.06)	12.97 ± 0.06	11.0(1.2)	Si
			2.70276	< 12.20	< 14.20	> –0.43	< 12.60	3.8(0.7)	Si
			2.70316	< 12.20	13.82(0.01)	–0.40(0.06)	12.75 ± 0.06	7.2(1.0)	Si
			2.70332	< 12.20	14.18(0.03)	–0.66(0.10)	13.20 ± 0.04	4.6(0.5)	Si
			2.70334	< 12.20	14.21(0.01)	–1.00(0.10)	13.71 ± 0.02	11.6(1.1)	Si
Q 0112+029	20.90(0.10)	–1.32(0.15)	2.42234	< 11.78	13.92(0.13)	–0.18(0.13)	12.56(0.24)	4.7(0.3)	S
			2.42248	< 11.78	14.04(0.11)	–0.35(0.12)	12.14(0.72)	6.8(0.8)	S
			2.42266	< 11.78	14.02(0.10)	–0.58(0.11)	12.21(0.59)	6.1(0.9)	S
			2.42277	< 11.78	14.16(0.08)	–0.37(0.09)	12.70(0.17)	3.7(0.3)	S
			2.42298	< 11.78	14.77(0.04)	–0.40(0.05)	13.66(0.06)	10.5(0.5)	S
			2.42323	< 11.78	14.65(0.04)	–0.38(0.05)	13.26(0.07)	6.3(0.3)	S
			2.42338	< 11.78	14.04(0.14)	–0.33(0.15)	13.20(0.08)	9.5(1.3)	S
			2.42353	< 12.22	13.97(0.06)	–1.13(0.09)	12.61(0.20)	2.5(0.6)	S
Q 0135–273	21.00(0.10)	–1.40(0.10)	2.79948	< 12.00	13.91(0.05)	–0.27(0.07)	12.78(0.25)	7.4(1.1)	S
			2.79960	< 12.00	14.14(0.10)	–0.33(0.12)	13.50(0.09)	0.1(0.1)	S
			2.79972	< 12.00	14.14(0.31)	–0.24(0.32)	13.39(0.12)	8.4(1.4)	S
			2.79982	< 12.00	14.08(0.30)	–0.24(0.32)	13.38(0.12)	5.5(1.0)	S
			2.79998	< 12.00	13.85(0.10)*	0.39(0.11)	13.69(0.06)	6.2(0.8)	S
			2.80010	< 12.00	14.05(0.38)*	0.08(0.38)	13.26(0.10)	3.9(0.4)	S
			2.80025	< 12.00	14.71(0.08)	–0.53(0.08)	13.85(0.07)	5.1(0.2)	S
Q 0405–443	21.15(0.15)	–1.41(0.15)	2.54967	< 11.70	12.99(0.27)	–0.84(0.82)	11.83(0.29)	0.3(0.1)	S
			2.54973	< 11.70	13.23(0.03)	–0.19(0.04)	12.75(0.05)	9.8(0.9)	S
			2.54992	< 11.70	14.56(0.02)	–0.23(0.02)	13.12(0.03)	5.3(0.2)	S
			2.55011	< 11.70	14.41(0.05)	–0.19(0.05)	13.21(0.04)	18.5(2.1)	S
			2.55049	< 11.70	13.76(0.11)	–0.09(0.12)	12.45(0.12)	9.4(2.2)	S
			2.55060	< 11.70	13.87(0.05)	–0.31(0.06)	12.38(0.07)	3.8(0.6)	S
			2.55078	< 11.70	14.10(0.05)	–0.48(0.06)	12.96(0.09)	7.8(1.3)	S
			2.55087	< 11.70	14.18(0.12)	–0.26(0.12)	13.16(0.12)	6.2(1.4)	S
			2.55097	< 11.70	14.30(0.06)	–0.31(0.06)	13.08(0.09)	4.5(0.4)	S
			2.55105	< 11.70	13.69(0.05)	–0.19(0.07)	12.75(0.03)	5.1(0.5)	S
			2.55124	< 11.70	13.86(0.03)	–0.29(0.04)	12.55(0.03)	5.9(0.5)	S
	20.45(0.10)	–2.04(0.11)	2.62101	< 11.64	12.92(0.02)	< 13.37	–0.23(0.04)	< 11.75	7.5(0.2)	Si
			2.62140	< 11.64	13.20(0.03)	< 13.37	–0.23(0.04)	< 11.75	5.4(0.2)	Si
			2.62158	< 11.64	13.47(0.02)	< 13.37	–0.28(0.03)	< 11.75	16.0(0.6)	Si
			2.62178	< 11.64	12.92(0.02)	< 13.67	–0.22(0.04)	< 11.75	4.4(0.2)	Si
			2.62219	< 11.64	12.02(0.05)	< 13.67	< +0.18	< 11.75	5.7(1.3)	Si
			2.62235	< 11.64	11.87(0.06)	< 13.67	< +0.33	< 11.75	2.0(1.3)	Si
			2.62287	< 11.64	12.98(0.02)	< 13.24	–0.55(0.06)	< 11.75	10.9(0.5)	Si
			2.62311	< 11.64	13.03(0.08)	< 13.24	–0.55(0.12)	< 11.75	6.9(0.9)	Si
			2.62320	< 11.64	12.96(0.08)	< 13.24	–0.55(0.13)	< 11.75	3.6(0.3)	Si
Q 0841+129	21.05(0.10)	–1.59(0.10)	2.37439	< 12.21	14.26(0.18)	–1.14(0.20)	12.91(0.14)	9.0(2.3)	S
			2.37455	< 12.21	14.43(0.12)	–0.60(0.23)	13.01(0.11)	7.2(1.3)	S
	20.80(0.10)	–1.60(0.10)	2.47604	< 12.21	13.47(0.27)	–0.51(0.34)	< 12.70	5.1(2.4)	S
			2.47621	< 12.21	14.42(0.05)	–0.26(0.07)	< 12.70	9.1(1.1)	S
			2.47642	< 12.21	13.35(0.27)	–0.40(0.30)	< 12.70	2.2(2.5)	S
Q 1037–270	19.70(0.05)	–0.31(0.06)	2.13910	12.51(0.02)	15.10(0.02)	14.65(0.01)	–0.20(0.03)	< 13.50	15.6(0.2)	Zn
			2.13951	12.46(0.02)	14.70(0.02)	14.23(0.01)	–0.05(0.04)	< 13.08	8.8(0.2)	Zn
Q 1101–264	19.50(0.04)	–1.07(0.06)	1.83817	< 11.68	12.29(0.09)	< 13.05	–0.85(0.18)	< 11.83	4.5(0.4)	Si
			1.83831	< 11.68	12.68(0.05)	< 13.05	–0.75(0.09)	< 11.83	10.3(0.3)	Si
			1.83854	< 11.68	13.33(0.02)	13.19(0.26)	–0.49(0.02)	< 11.83	5.8(0.1)	Si
			1.83871	< 11.68	13.21(0.02)	13.12(0.36)	–0.49(0.03)	< 11.83	9.4(0.2)	Si
			1.83890	< 11.68	13.61(0.02)	13.32(0.19)	–0.45(0.02)	< 11.83	5.4(0.1)	Si
			1.83915	< 11.68	12.77(0.05)	< 13.05	–0.23(0.05)	b	5.6(0.2)	Si
			1.83925	< 11.68	12.50(0.28)	< 13.05	–0.15(0.28)	b	2.0(0.2)	Si
			1.83933	< 11.68	12.44(0.26)	< 13.05	–0.42(0.26)	b	5.0(0.5)	Si
Q 1117–134	20.95(0.10)	–1.42(0.14)	3.35027	< 12.76	14.78(0.03)	b	–0.27(0.06)	< 13.66	6.9(0.4)	Zn
			3.35046	< 12.45	14.68(0.05)	b	–0.21(0.06)	< 13.31	6.5(0.6)	Zn
			3.35067	< 12.45	14.26(0.05)	b	> –0.47	< 13.29	6.2(0.3)	Zn
Q 1157+014	21.80(0.10)	–1.40(0.10)	1.94311	< 12.15	14.13(0.08)	–1.40(0.30)	12.36(0.14)	3.9(1.3)	Si
			1.94318	< 12.15	14.22(0.08)	–0.96(0.13)	12.21(0.23)	3.6(1.1)	Si
			1.94354	< 12.15	15.32(0.04)	–0.67(0.05)	13.91(0.04)	28.9(1.4)	Si
			1.94346	< 12.15	15.09(0.03)	–1.16(0.06)	13.74(0.04)	6.0(0.4)	Si
			1.94361	< 12.15	14.75(0.23)	–1.10(0.31)	13.00(1.37)	6.1(1.5)	Si
			1.94375	< 12.15	15.39(0.03)	–1.21(0.04)	14.08(0.18)	5.6(0.0)	Si
			1.94403	< 12.15	15.26(0.01)	–1.07(0.02)	13.87(0.02)	7.2(0.0)	Si
			1.94385	< 12.15	14.89(0.03)	–0.92(0.05)	13.96(0.03)	8.1(0.5)	Si
			1.94426	< 12.15	14.07(0.69)	13.14(0.06)	10.3(0.0)	Si
Q 1223+178	21.40(0.10)	–1.63(0.11)	2.46530	< 12.30	14.90(0.02)	14.56(0.03)	–0.12(0.04)	13.63(0.02)	10.3(0.3)	Zn
			2.46559	< 12.30	14.78(0.03)	14.54(0.04)	+0.02(0.06)	< 13.42	14.0(0.8)	Zn
			2.46607	< 12.30	15.22(0.02)	14.82(0.02)	–0.05(0.03)	< 13.04	14.7(0.3)	Zn
			2.46628	< 12.30	14.13(0.09)	< 13.85	< 12.55	4.3(0.7)	Zn
Q 1337+113	20.12(0.05)	–1.81(0.07)	2.50766	< 12.45	12.93(0.06)	b	–0.58(0.09)	< 12.55	5.0(1.3)	Si
			2.50792	< 12.45	13.82(0.04)	b	–0.40(0.04)	< 12.55	6.5(0.2)	Si
	21.00(0.08)	–1.86(0.10)	2.79557	< 12.40	13.90(0.16)	–0.22(0.17)	b	12.8(1.6)	Si
			2.79584	< 12.40	14.63(0.04)	–0.34(0.04)	b	6.6(0.3)	Si
Q 1451+123	20.40(0.10)	–2.27(0.14)	2.46897	< 12.75	13.23(0.09)	< 13.55	–0.21(0.09)	b	6.7(0.8)	Si
			2.46921	< 12.75	13.50(0.11)	< 13.55	–0.26(0.11)	b	5.7(0.5)	Si
	20.20(0.20)	–2.10(0.21)	3.17081	< 12.65	13.31(0.06)	–0.29(0.14			

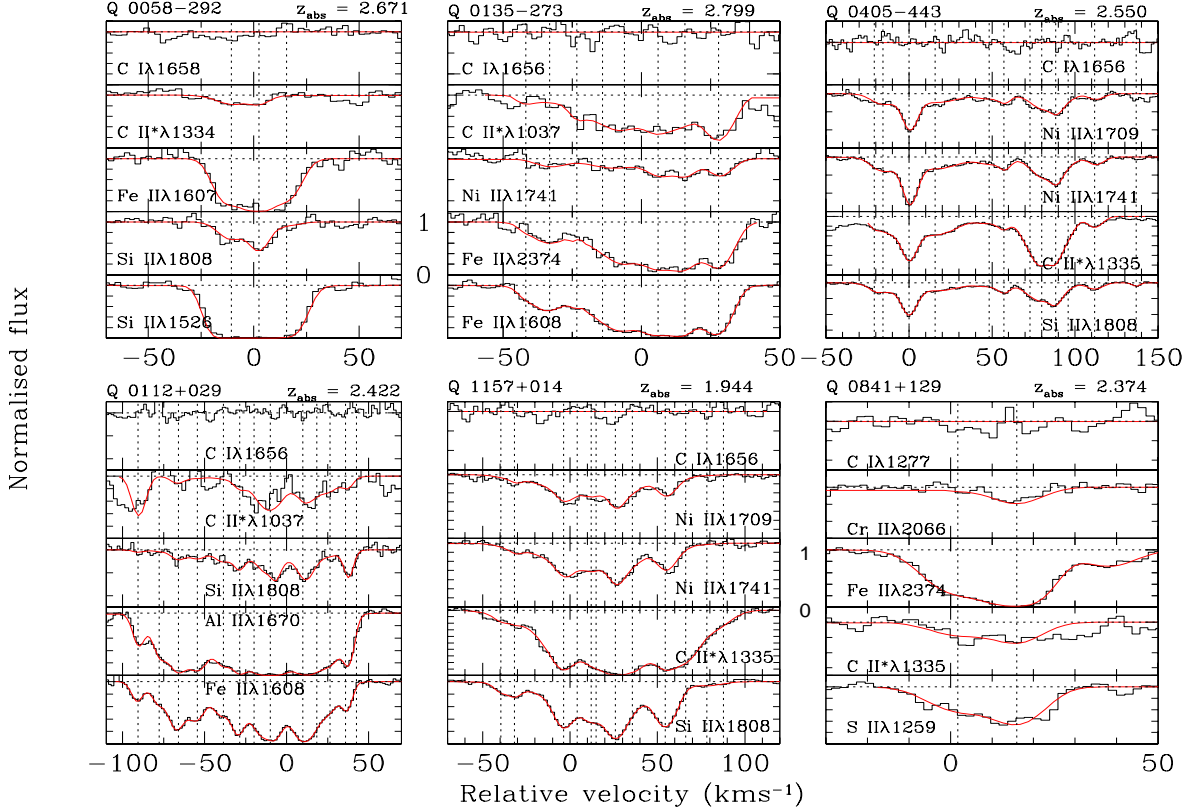


Figure 14. Voigt profile fits to systems with C II* absorption line and without H₂ or C I absorption lines. In each panel, the histogram gives the observed spectrum and the continuous curve is the best fitted multicomponent Voigt profile. The vertical dotted lines mark the locations of individual components.

$-2.0 \leq Z_{\odot} \leq -1.5$, are lower than what would be expected from CNM gas and are consistent with WNM (or low density) gas. Interestingly these upper limits are lower than that seen in high latitude Galactic sightlines that are believed to be predominantly WNM gas. This means that the electron density (and therefore probably the total particle density) in these DLAs is probably quite small.

6.3 Systems with H₂ detection

Systems with H₂ detections (marked as filled circles in Fig. 15) have $N(\text{C II}^*)/N(\text{C II})$ consistent with CNM. We compute the allowed range of n_{H} in these components using $N(\text{C II}^*)$, $N(\text{S II})$, n_e from the C I excitation and $T = T_{01}$ if available or $T = 100$ K (see Eq.7). The results are summarised in Column 6 of Table 4. This Table also gives upper limits on n_{H} for components without H₂ in systems that show H₂. It is to be remembered that we assume $[\text{C}/\text{S}]$ in DLAs is $[\text{C}/\text{S}]_{\odot}$. Realistically Carbon can be underabundant by up to a factor of 2. In that case the density will be higher than what we quote in the table. From Table 3 and 4 it is clear that for the H₂ components toward Q0347–383, Q0551–366 and Q1232+082 the value of n_{H} derived from both methods agree well. Such a comparison is not possible for the components toward Q0013–004 and Q0405–383 as C II* is blended in the former case and C I is not detected in the latter case. In the case of Q1444+014 the derived hydrogen density based on C II* is lower than that derived

Table 6. Systems without H₂ detection

QSO	z_{abs}	$\log x(\text{Al III})$	n_{H} (cm^{-3})			
			CNM ¹	WMN ²	Ionized ³	Max ⁴
Q 0058 – 292	2.671	3.1	1.2	0.3	<3
Q 0112 – 306	2.422	-1.46	24.4	9.6	2.3	<15
Q 0135 – 273	2.799	-1.86	60.0	23.4	5.6	<5
Q 0405 – 443	2.550	-1.58	7.3	1.8	0.4	<4
Q 0841 + 129	2.374	-1.16	11.3	2.8	0.7	<22
Q 1157 + 014	1.944	-1.68	16.3	4.0	1.0	<3
Q 1223 + 178	2.465	-1.35	9.4	2.3	0.6	<2

¹ $T = 100$ K and $n_e/n_{\text{H}} = 0.001$; ² $T = 8000$ K and $n_e/n_{\text{H}} = 0.01$

³ $T = 10^4$ K and $n_e/n_{\text{H}} = 0.1$; ⁴ from H₂ equilibrium formation

using C I fine-structure excitation. However, in this system, Ledoux et al. (2003) have found a 5 km/s shift between the C I absorption line and that of singly ionized species. In addition these components showing relative depletion of Si with respect to S, it is possible that we have over estimated $N(\text{C II})$. In summary, the n_{H} estimates based on the two methods are approximately consistent with one another. The excitation of the fine-structure levels of C I and C II in the components with H₂ detection are consistent with high density and low temperature CNM gas.

6.4 Systems without H₂ detection

In this Section we focus our attention on the 7 systems in our sample that show C II* without H₂. These systems do not show detectable C I absorption lines except the high-

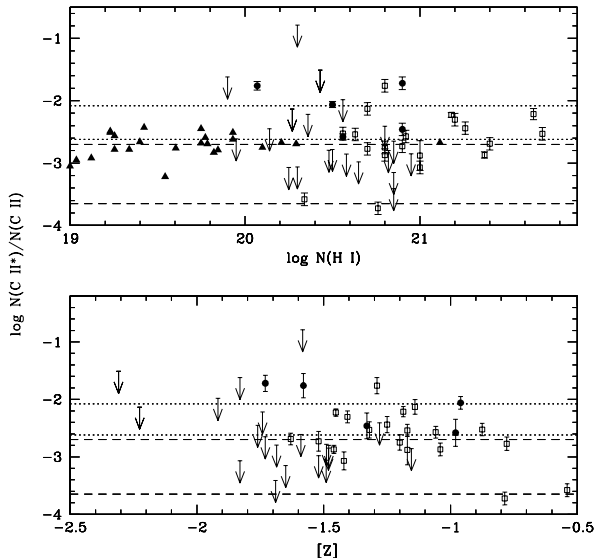


Figure 15. The average (over the whole profile) $N(\text{C II}^*)/N(\text{C II})$ ratio in DLAs (combining our sample to measures by Wolfe et al., 2003a, 2003b) is plotted against $\log N(\text{H I})$ (upper panel) and the metallicity Z (lower panel). The dotted lines show the expected range of values observed in the CNM gas with metallicity and dust-content ranging from that observed in the Galactic ISM to that of a typical DLA. The dashed lines give the corresponding range for the WNM gas. Filled circles and open squares are respectively for systems with and without H_2 detections. In the top panel the filled triangles are the observations of Lehner et al. (2004) along high latitude Galactic sightlines with low H_2 content. Most of the points with $\log N(\text{H I}) \leq 20.0$ are from intermediate or high velocity clouds in the Galactic halo.

metallicity system at $z_{\text{abs}} = 2.1391$ toward Tol 1037–270. Apart from the $z_{\text{abs}} = 1.943$ system toward Q 1157+014 that show 21 cm absorption line (Wolfe et al. 1981) there is no independent constraint on T and n_{H} . The identification of C II^* at $z_{\text{abs}} = 2.422$ toward Q 0112 + 029 and $z_{\text{abs}} = 2.799$ toward Q 0135 – 273 is based on $\text{C II}^* \lambda 1037$ absorption line. These lines are well inside the Lyman- α forest and possible contamination by intervening H I absorption cannot be ruled out. For the rest of the systems, the identification and estimation of the C II^* column density are secure.

We detect Al III absorption lines in the 6 (out of 7) systems for which our spectra cover the expected wavelength range of the redshifted Al III transitions. We estimate the fraction of Al in Al III using the observed metallicity and the observed $N(\text{Al III})$, assuming no depletion and solar relative abundances. Results are summarised in Table 6. From the Table, it can be seen that 1–7 % of Al is twice ionized. Using photoionization models from “CLOUDY” we derive a typical ionization parameter $-3 \leq \log U \leq -2$ if the gas originates from a single slab irradiated by stellar spectrum with an effective black-body temperature of 30,000–40,000 K (also see Fig. 1 in Izotov et al. 2001). This implies that the average n_e/n_{H} ratio along the line of sight is typically in the range 0.3 to 0.9. Thus there are enough electrons in the cloud so that collisions with electrons are dominant in the excitation of C II^* .

The average density, n_{H} , is derived using Eq. 7 and as-

suming three possible combinations of T and n_e/n_{H} . The results are summarised in Table 6. When we use no additional constraints, the C II^* observations alone are consistent with the gas having high density and low temperature (see Column 4 of Table 6).

The last column in the table gives the upper limit on n_{H} that will keep the equilibrium abundance of H_2 below our detection limit (i.e. $N(\text{H}_2) \leq 10^{14} \text{ cm}^{-2}$). This value is computed using simple formation equilibrium of optically thin H_2 (Jura 1975)

$$n_{\text{H}} = \frac{0.11\beta(0)N(\text{H}_2)}{RN(\text{HI})} \quad (8)$$

with, R and $\beta(0)$, respectively, the formation and photo-destruction rates of H_2 . In the case of the ISM, $R \simeq 3 \times 10^{-17} \text{ s}^{-1} \text{ cm}^{-3}$ and $\beta(0) \sim 5 \times 10^{-10} \text{ s}^{-1}$. We use the ISM value of R scaled by the dust content measured in the systems. It can be seen from Table 6 that for a moderate radiation field (like the ISM mean field) n_{H} derived using C II^* for the CNM like parameters is usually higher than the upper limit obtained based on the H_2 equilibrium formation. In addition, the expected electron density for the $T = 100$ K gas (assuming a n_e/n_{H} ratio as seen in CNM) is higher than 10^{-2} cm^{-3} . At such electron densities, C I should be detectable. This is inconsistent with the non-detection of C I in these systems. This problem of CNM gas producing very small amount of C I is already recognized in the literature (Liszt et al. 2002; Wolfe et al. 2003).

We notice that the absence of C I and H_2 in these systems is consistent with the gas originating either from the WNM gas or from the ionized gas. As pointed out above, the strength of the Al III absorption lines seen in these systems are consistent with the gas density being less than the one expected for the CNM.

Thus, if one uses only C II^* absorption line then the results are consistent with these systems originating from CNM gas. However the absence of H_2 and C I absorption lines together with the presence of Al III following the profiles of singly ionized gas is inconsistent with standard CNM solutions. Thus most of the DLAs without H_2 are consistent with them originating from low density, high temperature and partially ionized gas.

6.5 $z_{\text{abs}} = 1.944$ toward Q 1157 + 014

Some of our conclusions of the previous Section can be ascertained in the case of the $z_{\text{abs}} = 1.944$ system toward Q 1157 + 014 as we have additional information on the kinetic temperature based on 21 cm absorption (Wolfe et al. 1981). The estimated spin temperature based on the recent measurement of $N(\text{H I})$ is $T = 865 \pm 190$ K (Kankar & Chergalur 2003). Fig. 16 shows the velocity plot of selected absorption lines in this system. The distribution of neutral, singly ionized and doubly ionized species in velocity space can be visualized easily. Using a Gaussian profile, we also show, in the bottom panel, the velocity range over which 21 cm absorption is seen. Whereas the UV absorption lines spread over more than 100 km s^{-1} , the 21 cm absorption originates from only a few of the components. There are components that do not possess 21cm absorption but show absorption due to UV transitions including that of C II^* . As expected, C II^* traces a wide range of physical conditions.

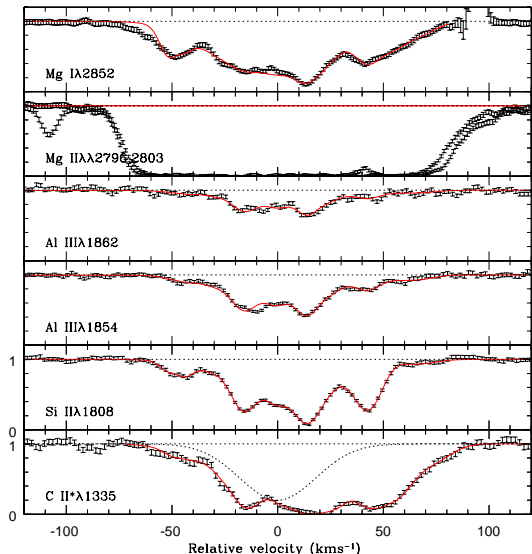


Figure 16. Velocity plot for the $z_{\text{abs}} = 1.944$ system toward Q 1157 + 014. The dotted Gaussian profile in the bottom panel is the reconstruction of the best fit Gaussian to the 21 cm observations of Wolfe et al. (1981). This is just to illustrate the velocity range over which cold hydrogen gas is detected.

Assuming the temperature of the gas that is producing the 21 cm absorption feature to be 100 K (or 200 K), we can derive from the 21 cm observation the H I column density in the component lying along the line of sight: $\sim 7 \times 10^{20} \text{ cm}^{-2}$ (or $1.4 \times 10^{21} \text{ cm}^{-2}$). This is approximately 15% (30%) of the total $N(\text{H I})$ measured from the damped Lyman- α line. This means that 85% (70%) of $N(\text{H I})$ along the line of sight is either warm or hot. From the Si II $\lambda 1808$ profile, we notice that $\sim 60\%$ of $N(\text{Si II})$ originate in the velocity space covered by the 21cm profile. We also notice that considerable fraction of Al III absorption originate from the velocity range covered by 21 cm absorption. Thus warm and ionized components seem to be co-spacial with the cold gas responsible for the 21 cm absorption. In addition we also notice Al III components with Si II and C II* absorption well separated from the 21 cm component. Thus part of the C II* absorption seen here originate from the WNM or WIM. Therefore, the non-detection of H₂ in this system can be easily explained as a consequence of most of the gas being at high temperature (and hence low density). The absence of H₂ from the cold 21 cm absorbing component could just be due to the low $N(\text{H I})$ associated with this component and the relatively low dust depletion.

7 DISCUSSION AND CONCLUSIONS

We have studied the physical conditions in damped Lyman- α systems (DLAs) using a sample of 33 systems toward 26 QSOs acquired for a recently completed survey of H₂ in DLAs by Ledoux et al. (2003). We use standard techniques to estimate the physical conditions prevailing in the gas. In this Section, we discuss some of the results and related issues.

7.1 High pressure of the H₂ gas

Our study shows that the H₂ components in DLAs trace Cold gas ($153 \pm 78 \text{ K}$) with relatively high pressure. The pressure in individual components (measured assuming a radiation field similar to our Galaxy) is in the range $824\text{--}30,000 \text{ cm}^{-3} \text{ K}$, a large fraction of the components being at high pressure. 42%, 20%, and 8% of the components have pressure in excess of $3000 \text{ cm}^{-3} \text{ K}$, $5000 \text{ cm}^{-3} \text{ K}$ and $10^4 \text{ cm}^{-3} \text{ K}$, respectively. Based on the profiles of singly ionized species we note the H₂ components arise in gas with a wide range of molecular content and ionization state much like what we see in the Galactic ISM.

This is not unexpected. Indeed, in the framework of a galactic two-phase medium, the stable pressure range for the gas is $460 \leq P/k (\text{cm}^{-2} \text{ K}) \leq 1750$ (Wolfe et al. 2003). Clearly the pressure we derive in the H₂ components are much higher than this. From Table 3 of Wolfire et al. (1995) it can be seen that for a given metallicity an increase in the dust-to-gas ratio can lead to an increase in the allowed range of pressure, whereas an increase in the metallicity reduces the allowed range of pressure due to enhanced cooling. For conditions typical of DLAs, that is for metallicities of $Z = -1.0$ and a dust-to-gas ratio ten times smaller than in the Galaxy, the stable pressure range is $1800\text{--}13000 \text{ cm}^{-3} \text{ s}^{-1}$ (Wolfire et al. 1995). Note that in the absence of any confining medium (or pressure equilibrium between different components) we expect such a high pressure gas to survive only for a short period of time (with a typical hydrodynamical time-scale of 10^6 years).

The pressure we infer depends very much on the intensity of the radiation field. A larger intensity implies and excess of UV pumping (on top of what we assume in our analysis) which, if taken into account, should reduce the hydrogen density derived using the C I fine-structure lines. At the same time, the temperature of the gas will increase due to photo-heating.

7.2 H₂ content

Ledoux et al. (2003) found that approximately 13–20% of DLAs show H₂ absorption lines with most of the H₂ components having column densities in the range $16.0 \leq \log N(\text{H}_2) (\text{cm}^{-2}) \leq 19.0$. In the case of the Galactic ISM, only a minor fraction of the clouds fall in this range. This is expected because, above $\log N(\text{H}_2) \simeq 16.0$, self-shielding drastically decreases the photo-dissociation rate. On the contrary, in the LMC and SMC, a large fraction of lines of sight have $16.0 \leq \log N(\text{H}_2) \leq 19.0$ (see Tumlinson et al., 2002). Thus the trend noticed in DLAs could just be a generic feature of gas with low dust content and metallicity. It is however important to remember that the molecular fraction given in Ledoux et al. (2003) is an average over the whole line of sight. The actual molecular fraction in individual components may be much larger. Thus the low values of $N(\text{H}_2)$ that are observed could just be a consequence of low $N(\text{H I})$ in the corresponding individual components. Indeed, consistent models of DLAs (Srianand et al. 2005) require H I column densities much less than the total $N(\text{H I})$ measured in DLAs with H₂. In addition, the absence of 21 cm absorption can be reconciled if the H₂ components have only part of the total H I (see below).

7.3 21 cm absorption

We have shown that detecting H_2 and C I absorption lines is an efficient way to trace the cold neutral gas in DLAs. H I 21 cm absorption line provides an independent way of detecting the CNM gas in DLAs. The detectability of 21 cm absorption line depends only on the amount of cold gas along the line of sight and the covering factor of the radio source. Thus, for a compact background source one can detect CNM gas with 21 cm without any bias from dust content or metallicity. At $z_{\text{abs}} \geq 2$, seven systems have been searched for 21 cm absorption and none have been detected (Kanekar & Chengalur 2003). Assuming $T = 200$ K for the CNM gas, these authors estimated the filling factor of the CNM gas to be ≤ 0.3 . This is consistent with what we derive from our H_2 survey. Over the redshift range covered by our survey there are three cases for which information on 21 cm absorption and H_2 content are available. To our surprise there seems to be no correlation between 21 cm absorption and H_2 absorption.

The $z_{\text{abs}} = 2.811$ system toward PKS 0528–255 show H_2 absorption in two distinct components without any corresponding 21 cm absorption (Carilli et al. 1996). The upper limit on $\tau(21\text{cm})$ gives $N(\text{H I}) \leq 5 \times 10^{20} \text{ cm}^{-2}$ if the kinetic temperature is similar to $T(\text{OPR})$ we measure. Thus H_2 and 21 cm observations can be consistent with one another if no more than 20% of the total H I column density is associated with the H_2 component. The $z_{\text{abs}} = 1.944$ system toward Q 1157+014 (Wolfe, Briggs & Jauncy, 1981; and discussion above) and $z_{\text{abs}} = 2.04$ towards PKS 0458-020 (Briggs et al., 1989; Ge & Bechtold, 1999) show strong 21 cm absorption but no C I or H_2 absorption. In these systems the absence of H_2 and C I absorption could be either due to low density in the cold H I component or to the presence of higher ambient radiation field.

7.4 C II* absorption

As pointed out before, C II* is detected in all the systems in which H_2 is seen. In fact, C II* is also detected in the three systems that show 21 cm absorption discussed in the previous Section. C II being the dominant ion of Carbon in the neutral gas, it is natural to expect C II* associated with both 21 cm and H_2 absorption. However, C II* is readily detected in warm neutral gas and even in ionized gas. The interpretation of the origin of the C II* absorption is not as straightforward as in the case of H_2 and C I. Thus, the nature of systems that do not show 21 cm absorption and/or H_2 absorption is a matter of debate. The systems that show C II* in our sample are consistent with them originating from the CNM gas. However, the absence of C I and H_2 (if we take the depletion as an indicator of the presence of dust) and the presence of Al III are also consistent with C II* absorption originating from the warm/partially ionized gas. Thus the frequency of occurrence of C II* provides a liberal upper limit on the CNM covering factor. A detailed investigation taking into account the constraints on the ionization state of the gas based on N II, Fe III or Al III will be important to derive the exact covering factor of CNM gas.

7.5 Star-Formation Rate

One of the main driver for the study of DLAs is to find out a way to recover the global star-formation history in a typical, moderately star-forming environment. The importance of DLAs in the paradigm of hierarchical structure formation can be appreciated from the fact that the mass density of baryonic matter in DLAs at $z_{\text{abs}} \sim 3$ is similar to that of stars at present epochs (Wolfe, 1995). Studies of Lyman- α and UV continuum emission from galaxies associated with DLAs usually result in star formation rates (or upper limits) of a few $M_{\odot} \text{ yr}^{-1}$ (Fynbo et al., 1999; Bunker et al., 1999; Kulkarni et al., 2001).

Wolfe et al. (2003a, 2003b) have proposed a novel idea of using the C II* cooling rate to infer the SFR in DLA galaxies. The idea is that if one assumes thermal equilibrium then the cooling rate inferred from C II* should be equal to the heating rate (through UV photons, Cosmic rays etc.,) driven by the local star-formation activity. Their detailed study suggests the star formation rate density of DLAs at high- z could be as high as that inferred based on Lyman break Galaxies. We confirm the presence of C II* in $\simeq 50\%$ of the DLAs in our sample. However, it is clear from the above discussion that one needs to unveil the nature of the partially ionized gas in order to have a handle on the heating rates.

In the local universe, star-formation is always related to molecular clouds. If DLAs are star-forming regions then the local star-formation has to be related to the mass of the molecular gas. Our survey shows that 13–20% of DLAs are associated with H_2 in absorption. We have not detected CO in any of these systems and HD is detected in only one system (Varshalavich et al., 2000). Clearly the dark molecular clouds where stars form in our Galaxy are not seen along QSO lines of sight. The UV radiation field inferred from the H_2 high-J excitation is similar to the Galactic mean field. Following Wolfe et al. (2003a,2003b) the SFR per unit comoving volume for DLAs is,

$$\begin{aligned} \dot{\rho}_{*} &= An_{\text{co}}(z) \langle \dot{\xi}(z) \rangle \\ &= f_d \langle \dot{\xi}(z) \rangle \left(\frac{A}{A_p} \right) \frac{dN}{dX} \end{aligned} \quad (9)$$

where, $\langle \dot{\xi}(z) \rangle$ is the average SFR per unit area at redshift z and A , A_p and $\frac{dN}{dX}$ are average physical cross-sectional, respectively, area, average projected area and number density of absorbers per unit absorption distance interval. f_d is the fraction of DLAs in which the UV radiation field is similar to the Galactic UV background (i.e., 0.13–0.20). Here we use the fact that our H_2 sample is a randomly chosen subsample of the whole population of DLAs and the presence of H_2 is independent of $N(\text{H I})$.

For an Einstein-de Sitter cosmology, $\frac{dN}{dX} = 3 \times 10^{-5}$ for the mean redshift of our sample (Storrie-Lombardi & Wolfe, 2000). Assuming $H_0 = 75 \text{ km s}^{-1} \text{ Mpc}^{-1}$, $A/A_p = 2$ and $\langle \dot{\xi}(z) \rangle = 4 \times 10^{-3} M_{\odot} \text{ yr}^{-1} \text{ kpc}^{-2}$ (typical for our Galaxy, see Kennicutt, 1998) we derive $\dot{\rho}_{*} \geq 0.03$ at $z_{\text{abs}} = 2.5$. This crude estimate already gives half the star formation rate density measured in Lyman break galaxies (Steidel et al., 1999). Recently, Hirashita & Ferrera (2005) have also arrived at similar conclusion. Thus it is of the utmost importance to understand the physics of the ISM in high- z DLAs in order to derive the cosmic star-formation budget correctly.

ACKNOWLEDGEMENTS

Results presented in this work are based on observations carried out at the European Southern Observatory (ESO) under prog. ID No. 65.P-0038, 65.O-0063, 66.A-0624, 67.A-0078, 68.A-0600 68.A-0106 and 70.A-0017 with the UVES spectrograph installed on the Very Large Telescope (VLT) at Cerro Paranal Observatory in Chile. RS and PPJ gratefully acknowledge support from the Indo-French Centre for the Promotion of Advanced Research (Centre Franco-Indien pour la Promotion de la Recherche Avancée) under contract No. 3004-3. GJF acknowledges the support of the NSF through AST 00-71180 and NASA with grant NAG5-12020. GJF and RS acknowledge the support from the DST/INT/US(NSF-RP0-115)/2002. GS would like to thank CCS, University of Kentucky for their two years of support. The hospitality of IUCAA is gratefully acknowledged.

REFERENCES

- Aracil, B., Petitjean, P., Pichon, C. & Bergeron, J. 2004, *A&A*, 419, 811
- Bahcall, J. N., Joss, P. C., Lynds, R., 1973, *ApJ*, 182, 95
- Bahcall, J. N., & Wolf, R. A. 1968, *ApJ*, 152, 701
- Bergeron, J., & Boissé, P. 1991, *A&A*, 243, 344
- Black, J. H., & van Dishoeck, E. F. 1987, *ApJ*, 322, 412
- Briggs, F. H., Wolfe, A. M., Liszt, H. S., Davis, M. M., & Turner, K. L. 1989, *ApJ*, 341, 650
- Browning M. K., Tumlinson J., & Shull J. M. 2003, *ApJ*, 582, 810
- Bunker, A. J., Warren, S. J., Clements, D.L., Williger, G.M., & Hewet, P. C. 1999, *MNRAS*, 309, 875
- Carilli C.L., Lane W., de Bruyn A.G., Braun R., & Miley G.K. 1996, *AJ*, 111, 1830
- Cazaux, S., & Tielens, A. G. G. M. 2002, *ApJ*, 575, L29
- Chaffee, F. H., Foltz, C. B., & Black, J. H. 1988, *ApJ*, 355, 584.
- Chand, H., Srianand, R., Petitjean, P., & Aracil, B. 2004, *A&A*, 417, 853
- Cui, J., Bechtold, J., Ge, J., Meyer, D. M., 2004, *AAS*, 20514501
- Dalgarno, A., Black, J. H., & Weisheit, J. C. 1973, *Astrophys. Lett.*, 14, 77
- Dekker H., D’Odorico S., Kaufer A., Delabre B., & Kotzlowski H. 2000, in Iye M., Moorwood A. F., eds, *Proc. SPIE Vol. 4008, Optical and IR telescope instrumentation and detectors*, p. 534
- Flower, D.R., & Watt, G. D. 1984, *MNRAS*, 209,25
- Forrey, R.C., Balakrishnan, N., Dalgarno, Alex, & Lepp, S. 1997, *ApJ*, 489, 1000
- Fynbo, J. U., Moller, P., & Warren, S. J. 1999, *MNRAS*, 305, 849
- Ge, J., & Bechtold, J. 1999, in Carilli C. L., Radford S. J. E., Menten K. M., & Langston G. I., eds., *Highly redshifted Radio Lines*, ASP Conf. Series, Vol. 156, p. 121
- Ge, J., & Bechtold, J. 1997, *ApJ*, 477, 73.
- Ge, J., Bechtold, J. & Black, J. H. A. 1997, *ApJ*, 434, 67
- Ge, J., Bechtold, J., & Kulkarni, V. P. 2001, *ApJ*, 547, 1
- Gerlich, G. 1990, *JChPh*, 92, 2377
- Hirashita, H., Ferrera, A., 2005, *MNRAS*, 356, 1529
- Haehnelt, M. G., Steinmetz, M., & Rauch, M. 1998, *ApJ*, 495,647
- Howk, J. C & Sembach, K. R. 1999, *ApJ*, 523, 141
- Heiles, C. 2001, *ApJ*, 551, L105
- Izotov, Y. I., Schaerer, D., & Charbonnel, C. 2001, *ApJ*, 549, 878.
- Jenkins, E. B., Jura, M., & Loewenstein, M. 1983, *ApJ*, 270, 1
- Jenkins, E. B., & Peimbert, A. 1997, *ApJ*, 477, 265
- Jenkins, E. B., & Shaya, E. J. 1979, *ApJ*, 231, 55
- Jenkins, E. B., & Tripp, T. M. 2001, *ApJ*, 137, 297
- Jura, M. 1975, *ApJ*, 197, 581
- Kanekar, N., Chengalur, J., 2003, *A&A*, 399, 857
- Keenan, F. P., Lennon, D. J., Johnson, C. R., & Kingston, A. E., 1986, *MNRAS*, 220, 571
- Kennicutt, R. C. 1998, *ApJ*, 498, 541
- Kulkarni, V. P. et al. 2001, *ApJ*, 551, 37
- Le Bourlot, J., 2000, *A&A*, 360, 656
- Le Brun, V., Bergeron, J., Boisse, P., & Deharveng, J. M. 1997, *A&A*, 321, 733
- Launay, J. M. & Roueff, E. 1977, *A&A*, 56, 289
- Lehner, N., Wakker, B. P., & Savage, B. D. 2004, *astro-ph/0407363*
- Ledoux, C., Petitjean, P., Bergeron, J., Wampler, E., & Srianand, R. 1998, *A&A*, 337, 51
- Ledoux, C., Petitjean, P., & Srianand, R. 2003, *MNRAS*, 346,209
- Ledoux, C., Srianand, R., & Petitjean, P. 2002, *A&A* 392, 781
- Levshakov, S. A., Dessauges-Zavadsky, M., D’Odorico, S., & Molero, P. 2002, *ApJ*, 565, 696
- Liszt, H. 2002, *A&A*, 389, 393
- Lu, L., Sargent, W. L. W., Barlow, T. A., Churchill, C. W., & Vogt, S. S. 1996, *ApJ*, 107, 475
- Mandy, M. E., & Martin, P. G. 1993, *ApJS*, 86, 199
- Morton D. C., & Dinerstein H. L. 1976, *ApJ*, 204, 1
- Meyer, D. M., Black, J. H., Chaffee, F. H., Foltz, G., York, D., 1986, *ApJ*, 308, 37
- Péquignot, D., & Aldrovandi, S. M. V. 1986, *A&A*, 161, 169
- Péquignot, D., Petitjean, P., & Boisson, C. 1991, *A&A*, 251, 680
- Péroux, C., Petitjean, P., Aracil, B., & Srianand, R. 2002, *New Astronomy*, 7, 577
- Petitjean, P., Ivanchik, A., Srianand, R., Aracil, B., Varshalovich, D., Chand, H., Rodrigues, E., Ledoux, C., & Boissé, P. 2004, *C. R. Physique*, 5(2004), 411-415.
- Petitjean, P., Srianand, R., & Ledoux, C. 2000, *A&A*, 364, L26
- Petitjean, P., Srianand, R., & Ledoux, C. 2002, *MNRAS*, 332, 383
- Pettini, M., Smith, L. J., King, D. L. & Hunstead, R. W. 1997, 486, 665
- Prochaska, J., & Wolfe, A. 1997, *ApJ*, 487, 73
- Prochaska, J., Wolfe, A. M., 1999 *ApJS*, 121, 369
- Quast, R., Baade, R., & Reimers, D. 2002, *A&A*, 386, 796
- Reimers D., Baade, R., Quast, R., & Levshakov, S.A. 2003, *A&A*, 410,785
- Roth, K. C., Bauer, J., 1999, *ApJ*, 515, 57
- Roy, N., Chengalur, J. N., Srianand, R., 2005, preprint
- Savage, B. D., Drake, J. F., Budich, W., & Bohlin, R. C. 1977, *ApJ*, 216, 291
- Savage B. D., Sembach K. R., 1996, *ARA&A*, 34, 279 *J. Phys. B*, 24, 2487
- Shaw, G., Ferland, G., Stancil, P., Srianand, R., 2004, *AAS*, 204.6120
- Shull, J. M., & van Steenberg, M. 1982, *ApJS*, 48, 95
- Silva, A. I., & Viegas, S. M. 2002, *MNRAS*, 329, 135
- Songaila, A et al., 1994, *Nature*, 371, 43
- Spitzer, L. Jr., Cochran, W. D., & Hirshfeld, A. 1974, *ApJS*, 28, 373
- Srianand, R., & Petitjean, P. 1998, *A&A*, 335, 33
- Srianand, R., Petitjean, P. 2001, *A&A*, 373, 816
- Srianand, R., Petitjean, P., & Ledoux, C. 2000, *Nature*, 408, 931
- Srianand, R., Shaw, G., Ferland, G., Petitjean, P., Ledoux, C., 2005, *MNRAS* submitted
- Sternberg, A., & Neufeld, D. A. 1999, *ApJ*, 516, 371
- Steidel, C. C. et al., 1999, *ApJ*, 519, 1
- Storrie-Lombardi, L. J., & Wolfe, A. M. 2000, *ApJ*, 543, 552
- Takahashi, J. 2001, *ApJ*, 561, 254
- Tiné, S., Lepp, S., Gredel, R., & Dalgarno, A. 1997, *ApJ*, 481, 282
- Tumlinson, J., Shull, J. M., Rachford, B. L., et al. 2002, *ApJ*, 566, 857
- Turner, J., Kirby-Docken K., & Dalgarno A. 1977, *ApJS*, 35, 281

- Varshalovich, D. A., Ivanchik, A. V., Petitjean, P., Srianand, R., & Ledoux, C. 2001, *AstL*, 27, 683
- Vladilo, G., Centurión, M., Bonifacio, P., & Howk, J. C. 2001, *ApJ*, 557, 1007
- Welty D. E., Hobbs, L. M., Lauroesch, J. T., Morton, D. C., Spitzer, L., & York, D. J. 1999, *ApJS*, 124, 465
- Welty, D. E., Hobbs, L. M., & Morton, D. C. 2002, *ApJS*, 147, 61.
- Wolfe A. M., 1995. in *QSO Absorption Lines*, Proc. ESO Workshop, ed. G. Meylan (Berlin:Springer), 13
- Wolfe, A. M., Briggs, F. H., & Jauncey, D. L. 1981, *ApJ*, 248, 460.
- Wolfe, A. M. & Prochaska, J. X. 2000, *ApJ*, 545, 603
- Wolfe, A. M. Prochaska, J. X., & Gawiser, E. 2003, *ApJ*, 593,215
- Wolfe, A. M., Gawiser, E., & Prochaska, J. X. 2003, *ApJ*, 593,235
- Wolfe, A. M., Howk, J. C., Gawiser, E., Prochaska, J. X., Lopez, S. 2004, *ApJ*, 615, 525
- Wolfire, M. G., Hollenbach, D., McKee, C. F., & Tielens, A. G. G. M. 1995, *ApJ*, 443, 152
- Wolfire, M. G., McKee, C. F., Hollenbach, D., & Tielens, A. G. G. M. 2003, *ApJ*, 587, 278